Inorganic Chemistry

Article

pubs.acs.org/IC

Oxoiron(IV) Tetramethylcyclam Complexes with Axial Carboxylate Ligands: Effect of Tethering the Carboxylate on Reactivity

Jennifer O. Bigelow,[†] Jason England,[†,∥] Johannes E. M. N. Klein,[†] Erik R. Farquhar,[†,∥] Jonathan R. Frisch,[†,∥] Marlène Martinho,[‡,∥] Debasish Mandal,[§] Eckard Münck,*[,‡] Sason Shaik,*[,§] and Lawrence Que, Jr.*[,†]

[†]Department of Chemistry and Center for Metals in Biocatalysis, University of Minnesota, Minneapolis, Minnesota 55455, United States

[‡]Department of Chemistry, Carnegie Mellon University, Pittsburgh, Pennsylvania 15213, United States

[§]Institute of Chemistry and the Lise Meitner-Minerva Center for Computational Quantum Chemistry, The Hebrew University of Jerusalem, 91904 Jerusalem, Israel

Supporting Information

ABSTRACT: Oxoiron(IV) species are implicated as reactive intermediates in nonheme monoiron oxygenases, often acting as the agent for hydrogen-atom transfer from substrate. A histidine is the most likely ligand *trans* to the oxo unit in most enzymes characterized thus far but is replaced by a carboxylate in the case of isopenicillin *N* synthase. As the effect of a *trans* carboxylate ligand on the properties of the oxoiron(IV) unit has not been systematically studied, we have synthesized and characterized four oxoiron(IV) complexes supported by the tetramethylcyclam (TMC) macrocycle and having a carboxylate ligand *trans* to the oxo unit. Two complexes have acetate or propionate axial ligands, while the other two have the carboxylate functionality tethered to the macrocyclic ligand framework by one or two methylene units. Interestingly, these four complexes exhibit substrate oxidation rates that differ by more than 100-fold, despite having $E_{p,c}$ values for the reduction of the Fe═O unit that span a range of only 130 mV. Eyring parameters for 1,4-cyclohexadiene oxidation show that reactivity differences originate from differences in activation enthalpy between complexes with tethered carboxylates and those with untethered carboxylates, in agreement with computational results. As noted previously for the initial subset of four complexes, the logarithms of the oxygen atom transfer rates of 11 complexes of the Fe^{IV}(O)TMC(X) series increase linearly with the observed $E_{p,c}$ values, reflecting the electrophilicity of the Fe═O unit. In contrast, no correlation with $E_{p,c}$ values is observed for the corresponding hydrogen atom transfer (HAT) reaction rates; instead, the HAT rates increase as the computed triplet−quintet spin state gap narrows, consistent with Shaik's two-state-reactivity model. In fact, the two complexes with untethered carboxylates are among the most reactive HAT agents in this series, demonstrating that the axial ligand can play a key role in tuning the HAT reactivity in a nonheme iron enzyme active site.

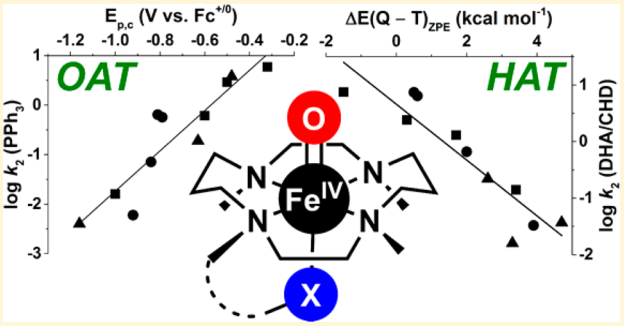

INTRODUCTION

Enzymes with mononuclear nonheme iron active sites utilize molecular oxygen as an oxidant to catalyze a wide variety of reactions in the biological world such as C−H bond hydroxylation and halogenation, C−C bond desaturation, and heterocyclic ring formation in the biosynthesis of essential metabolites and antibiotics.[1,2] Despite this array of reactivity, many share a common 2-His-1-carboxylate facial triad active site[3−5] that supports formation of a common oxoiron(IV) oxidant, which has been trapped and characterized for several enzymes.[6−15] These high-valent intermediates are proposed to abstract a hydrogen atom from substrate, generating a carbon-based substrate radical that then reacts to form C−O, C−halogen, C−S, or C═C bonds.[2,6−15] However, the exact factors controlling the reactivity of these oxoiron(IV) species are still unknown. One factor that has attracted little attention thus far is what possible role a carboxylate ligand bound to the oxoiron(IV) unit may play in modulating the reactivity of this unit. For most of the nonheme iron enzymes with an active site consisting of a 2-His-1-carboxylate facial triad, the likely site for O_2 binding, and hence the site at which the oxo is formed, is *trans* to a His residue.[2−5] However, in at least the case of isopenicillin *N* synthase, NO has been shown to bind *trans* to a carboxylate residue; therefore, O_2 and the resulting oxo moiety derived therefrom would be expected to be *trans* to a carboxylate ligand.[16−19] The effects of introducing a carboxylate *trans* to a nonheme oxoiron(IV) unit on its reactivity have not

Received: November 4, 2016
Published: March 3, 2017

DOI: 10.1021/acs.inorgchem.6b02659
Inorg. Chem. 2017, 56, 3287−3301

been investigated in detail, and the goal of this study is to shed light on what role a carboxylate ligand may play at this position.

Synthetic efforts to model a nonheme oxoiron(IV) unit since 2000 have investigated how factors such as spin state, electronics, and sterics can affect reactivity.[20−24] Among these studies, the most systematic one has involved the tetramethylcyclam (TMC) macrocycle as a ligand platform to obtain an array of oxoiron(IV) complexes that vary with respect to the nature of the axial ligand[25−28] and, more recently, with respect to the macrocyclic face to which the oxo atom is placed.[29] Early work by Sastri et al. indicated that the rates of oxygen atom transfer (OAT) decreased with increasing electron-donating capability of an axial ligand, showing the expected electrophilic trend. In contrast, the rate of hydrogen atom transfer (HAT) *increased* with the electron-donating ability of the axial ligand, revealing what Sastri et al. called an antielectrophilic trend.[26] The electron-donating capability of the *trans* axial ligand was reflected experimentally by the $E_{p,c}$ (cathodic peak potential) values of the oxoiron(IV) complexes obtained and computationally by the calculated Δq_{CT} value (the amount of charge transferred from the axial ligand to the Fe═O unit).[26,30,31] Complexes of this type have been proposed to engage in two-state reactivity (TSR),[32−34] wherein both OAT and HAT reactions occur on the more reactive $S = 2$ spin surface.[26,30,31] The antielectrophilic trend observed for HAT by Sastri et al. was thus attributed to the accessibility of the $S = 2$ spin state.[26] The smaller the gap, the greater the contribution of the $S = 2$ transition state to the reaction, which was lower in energy than the $S = 1$ transition state. Notably, reactions proceeding via the $S = 2$ potential energy surface are proposed to be intrinsically lower in energy due to exchange enhanced reactivity.[35] The $S = 1/S = 2$ gap would then be controlled by the electron-donating ability of the axial ligand, so that the complexes with the more electron donating ligands would give rise to smaller gaps, leading in turn to complexes with higher HAT reactivity.[26]

The explanation of this correlation was recently challenged by data obtained for the conjugate acid−base pair **1** and **2** (see Scheme 1), which are also supported by ligands based on the TMC framework to which the axial donor is appended.[28] While **2** has an axial ligand much more electron donating than **1**, on the basis of their $E_{p,c}$ values determined by cyclic voltammetry, **1** exhibits faster HAT rates than **2**. This case of two very similar oxoiron(IV) complexes that only differ in the loss of a proton indicates that the reactivity of such complexes may be based on factors other than the electron-donating ability of the axial ligand alone.

In response to these observations, a refined model was proposed[30] in which the originally observed antielectrophilic trend was attributed to an increased H atom tunneling contribution for the complexes with more electron donating ligands *trans* to the oxo donor.[26] Nevertheless, all reactions are still proposed to proceed on the $S = 2$ spin surface rendering TSR operational.[30] Tunneling contributions were predicted to give rise to kinetic isotope effects (KIE, k_H/k_D) in the range of 10−60 for HAT reactions on the $S = 2$ spin surface, in agreement with available experimental data.[26,30] On the other hand, KIE values on the order of hundreds were calculated for the $S = 1$ spin surface, making contributions of this spin state to the reaction unlikely. The study predicts that more electron donating ligands will have larger KIE values for HAT, while OAT cannot proceed through a tunneling path due to the much larger mass of the oxygen atom.

Scheme 1. Oxoiron(IV) Complexes Supported by the TMC Macrocycle Relevant to This Study

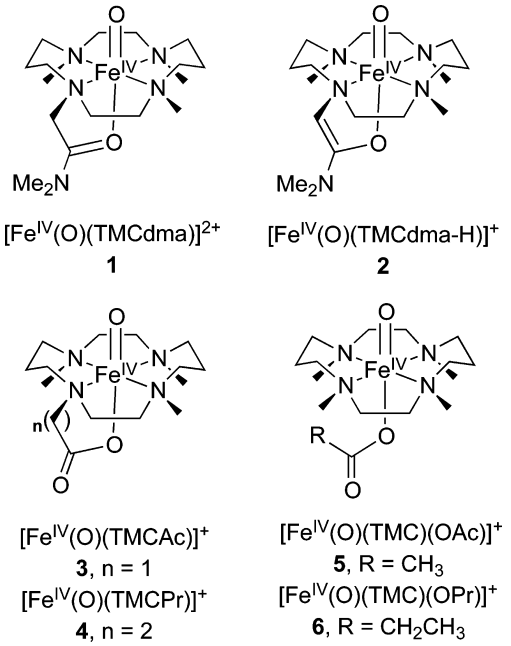

Herein, we extend our investigation of TMC-based oxoiron(IV) complexes to a series of complexes with axially bound carboxylate ligands (Scheme 1). Two complexes, **3** and **4**, respectively, possess acetate and propionate donors appended to the TMC macrocycle in place of a methyl substituent, while **5** and **6** are the corresponding complexes with untethered acetate and propionate anions as respective axial ligands. Our study of the oxidative reactivity of **3**−**6** shows that tethering the carboxylate ligands can result in a greater than a 100-fold decrease in both HAT and OAT rates. When these data are viewed within the broader context of 11 Fe^{IV}(O)TMC complexes characterized to date, the OAT values correlate with the $E_{p,c}$ values measured for the complexes, consistent with the electrophilic trend found by Sastri et al. for an initial subset of four complexes.[26] However, the antielectrophilic trend originally observed for HAT reactivity does not hold when it is applied to the entire data set, as tethering the axial carboxylate ligand appears to constrain the ability of the oxoiron(IV) unit to effect HAT without significantly affecting the $E_{p,c}$ values. On the other hand, the HAT rates for the entire set of Fe^{IV}(O)TMC complexes can be correlated primarily with the calculated spin state energy differences ($\Delta E(Q\text{-}T)_{ZPE}$ with solvation correction) of the oxoiron(IV) reactants, thereby providing further validation for Shaik's TSR model.[26,30]

EXPERIMENTAL SECTION

General Considerations. All reagents, including anhydrous solvents, were purchased from Aldrich and used as received unless noted otherwise. Iodosobenzene (PhIO),[36] its ^{18}O-labeled isotopomer PhI^{18}O, $Fe(OTf)_2(CH_3CN)_2$,[37,38] 1,4,8-trimethyl-1,4,8,11-tetraazacyclotetradecane,[39,40] 4,8,11-trimethyl-1,4,8,11-tetraazacyclotetradecane-1-acetic acid tetrahydrochloride salt (TMCAcH·4HCl),[41] and NBu_4OPr[42] were all prepared according to published procedures. [Fe^{II}TMC(OTf)](OTf) was prepared by a modified published procedure,[43] as follows: generally, 1 mmol of $Fe(OTf)_2(CH_3CN)_2$ was dissolved in dichloromethane with 1 mmol of TMC. This was stirred for 2−3 h before being filtered into diethyl ether. A precipitate formed immediately. The solution was filtered and the solid collected.

DOI: 10.1021/acs.inorgchem.6b02659
Inorg. Chem. 2017, 56, 3287−3301

The solid was dissolved in dichloromethane and set up for vapor diffusion with diethyl ether in a −40 °C freezer. After several days, the solution was filtered and the solid collected. A typical yield was 64%. TMC was purchased from Angene International Limited or Strem. Triphenylphosphine was purified by dissolving in hexane and running through a silica gel column. 9,10-Dihydroanthracene (DHA) was purified by a published procedure,[44] and d_4-DHA was also synthesized by a published procedure.[45]

All moisture- and oxygen-sensitive compounds were prepared using standard high-vacuum-line, Schlenk, or cannula techniques. A standard nitrogen-filled glovebox was used for any subsequent manipulation and storage of these compounds. NMR spectra were recorded using Varian Inova 500 and 300 MHz spectrometers. Chemical shifts (ppm) were referenced to the residual protic solvent peaks. Elemental analyses were performed by Atlantic Microlab (Norcross, GA). UV−visible studies were performed using a HP8453A diode array spectrometer equipped with a cryostat from Unisoku Scientific Instruments (Osaka, Japan). Electrospray ionization mass spectrometry experiments were carried out on a Bruker BioTOF II mass spectrometer using a spray chamber voltage of 4000 V and a gas carrier temperature of 60 °C. FT-IR spectra were recorded in CH_3CN solution at ambient temperature in a CaF_2 solution cell (International Crystal Laboratories), using an Avatar 370 spectrometer (ThermoNicolet).

Synthetic Procedures. *TMCPrH·4HCl.* To a solution of Me_3cyclam (1.00 g, 4.13 mmol) in acetonitrile (40 mL) was added 20 equiv of *tert*-butyl acrylate (12.1 mL, 82.5 mmol), and the resulting mixture was stirred under argon for 72 h. Subsequently, all volatiles were removed under vacuum to provide a yellow oil. ^{1}H NMR ($CDCl_3$, 500 MHz): δ 2.76 (t, 2H, NCH_2CCO_2), 2.54 (m, 4H, NCH_2), 2.44 (m, 12H, NCH_2), 2.35 (t, 2H, CH_2CO_2), 2.22 (s, 3H, NMe), 2.21 (s, 3H, NMe), 2.20 (s, 3H, NMe), 1.64 (p, 4H, $NCCH_2CN$), 1.44 (s, 9H, ^{t}BuO). ^{13}C NMR ($CDCl_3$, 125 MHz): δ 172.28, 54.71, 54.45, 54.25, 53.69, 53.62, 53.42, 50.58, 50.47, 50.22, 43.62, 43.58, 43.29, 33.18, 28.15, 24.40. MS (+ESI): m/z 371.5 [$(M + H)^+$].

The ester was dissolved in trifluoroacetic acid (40 mL) and stirred in a sealed flask, at ambient temperature, for 96 h. Removal of all volatiles yielded a brown oil, from which an off-white solid could be obtained by trituration with diethyl ether overnight. This solid was isolated by filtration, washed with further diethyl ether, and air-dried. ^{1}H NMR (D_2O, 500 MHz): δ 3.51 (m, 2H, NCH_2), 3.43 (m, 4H, NCH_2), 3.20 (m, 6H, NCH_2), 3.12 (t, 2H, NCH_2), 2.97 (t, 2H, NCH_2CCO_2), 2.86 (t, 2H, NCH_2), 2.83 (s, 3H, NMe), 2.82 (s, 3H, NMe), 2.78 (s, 3H, NMe), 2.60 (t, 2H, CH_2CO_2), 2.01 (m, 2H, $NCCH_2CN$), 1.83 (m, 2H, $NCCH_2CN$). MS (+ESI): m/z 315.2 [$(TMCPrA + 2H)^+$]. Anal. Calcd (found) for $C_{24}H_{38}F_{12}N_4O_{10}$: C, 37.41 (37.42); H, 4.97 (4.94); F, 29.59 (29.37); N, 7.27 (7.40); O, 20.76 (20.94).

Dissolution of the trifluoroacetate salt in methanol and addition of concentrated hydrochloric acid caused precipitation of a solid, which was isolated by filtration, washed with methanol, followed by diethyl ether, and air-dried to give the title compound as a white powder (2.44 g, 77% overall). ^{1}H NMR (D_2O, 500 MHz): δ 3.58 (m, 2H, CH_2), 3.50 (m, 4H, CH_2), 3.26 (m, 8H, NCH_2), 3.07 (t, 2H, NCH_2), 2.99 (t, 2H, NCH_2CCO_2), 2.86 (s, 3H, NMe), 2.85 (s, 3H, NMe), 2.81 (s, 3H, NMe), 2.65 (t, 2H, CH_2CO_2), 2.05 (m, 2H, $NCCH_2CN$), 1.90 (m, 2H, $NCCH_2CN$). Anal. Calcd (found) for $C_{16}H_{38}Cl_4N_4O_2·3H_2O$: C, 37.36 (37.76); H, 8.62 (8.42); Cl, 27.57 (27.29); N, 10.89 (10.87).

Synthesis of Iron(II) Complexes (Numbered according to the Oxoiron(IV) Numbering Scheme in Scheme 1 Followed by an Asterisk). [3][BPh$_4$].* To a methanolic suspension of TMCAcH·4HCl (0.63 g, 1.41 mmol) was added 4 equiv of sodium methoxide (0.30 g, 5.63 mmol). After 15 min of stirring, all volatiles were removed to yield a residue, to which dichloromethane was added. This dissolved the monoprotonated ligand, but not the sodium chloride byproduct, which was removed by filtration. The dichloromethane extracts were reduced to dryness to provide TMCAcH as a waxy solid, which was then dissolved in methanol, treated with triethylamine (0.65 g, 6.40 mmol) and $Fe(OTf)_2(CH_3CN)_2$ (0.56 g, 1.28 mmol), and stirred for 12 h. Subsequent addition of sodium tetraphenylborate (0.44 g, 1.28 mmol) caused precipitation of a white powder, which was isolated by filtration, washed with methanol and diethyl ether, and dried under vacuum to give 0.77 g of product (89% yield). ^{1}H NMR (CD_3CN, all peaks appear as broad singlets): δ 342.9 (1H, CH_2), 337.3 (1H, CH_2), 335.8 (1H, CH_2), 322.6 (1H, CH_2), 193.2 (1H, CH_2), 167.0 (1H, CH_2), 155.2 (1H, CH_2), 146.3 (2H, CH_2), 131.8 (3H, N*Me*), 96.0 (3H, N*Me*), 88.2 (2H, CH_2), 81.7 (3H, N*Me*), 63.1 (1H, CH_2), 35.3 (1H, CH_2), 22.9 (3H, N*Me*), 7.4 (8H, BPh_4), 7.0 (8H, BPh_4), 6.9 (4H, BPh_4), −13.5 (1H, CH_2), −30.1 (1H, CH_2), −58.1 (1H, CH_2). MS (+ESI): m/z 355.3 [$(M - BPh_4)^+$]. Anal. Calcd (found) for $C_{39}H_{51}BFeN_4O_2$: C, 69.45 (69.59); H, 7.62 (7.66); N, 8.31 (8.18). The analogous [**3***][$B(C_6F_5)_4$] complex was synthesized through a similar procedure, except $NaBPh_4$ was replaced with $Li[B(C_6F_5)_4]·Et_2O$.

[4][BPh$_4$].* This complex was prepared in a fashion analogous to that for [**3***][BPh_4], using 0.60 g (1.30 mmol) of TMCPrH·4HCl and 0.21 g (5.21 mmol) of sodium hydroxide to provide the ligand TMCPrH and 0.60 g (5.92 mmol) of triethylamine, 0.52 g (1.18 mmol) of $Fe(OTf)_2(CH_3CN)_2$, and 0.41 g (1.18 mmol) of sodium tetraphenylborate in the subsequent complexation. The product was obtained as a white powder in 78% yield (0.70 g). ^{1}H NMR (CD_3CN, all peaks appear as broad singlets): δ 308.7 (1H, CH_2), 294.8 (2H, CH_2), 282.7 (1H, CH_2), 275.8 (1H, CH_2), 153.9 (1H, CH_2), 148.4 (1H, CH_2), 132.6 (3H, N*Me*), 121.0 (1H, CH_2), 112.1 (1H, CH_2), 103.1 (3H, N*Me*), 97.1 (3H, N*Me*), 68.0 (2H, CH_2), 51.2 (1H, CH_2), 34.2 (1H, CH_2), 26.9 (1H, CH_2), 20.7 (1H, CH_2), 15.6 (1H, CH_2), 12.6 (1H, CH_2), 7.4 (8H, BPh_4), 7.0 (8H, BPh_4), 6.9 (4H, BPh_4), −1.4 (1H, CH_2), −5.8 (1H, CH_2), −16.0 (1H, CH_2), −19.3 (1H, CH_2). MS (+ESI): m/z 369.1 [$(M - BPh_4)^+$]. Anal. Calcd (found) for $C_{40}H_{53}BFeN_4O_2$: C, 69.78 (69.83); H, 7.76 (7.78); N, 8.14 (8.02). The analogous [**4***][$B(C_6F_5)_4$] complex was synthesized through a similar procedure, except for the replacement of $NaBPh_4$ with $Li[B(C_6F_5)_4]·Et_2O$.

[5][BPh$_4$].* A mixture of TMC (0.20 g, 0.78 mmol) and iron(II) acetate (0.14 g, 0.78 mmol) were stirred together in methanol (10 mL) for 12 h. Subsequent to filtration, the filtrate was treated with sodium tetraphenylborate (0.27 g, 0.78 mmol), which caused a white precipitate to form. This solid was isolated by filtration, washed with methanol (2 × 5 mL), and dried under vacuum to give the product as a white powder (0.45 g, 84%). ^{1}H NMR (CD_3CN, all peaks appear as broad singlets): δ 274.3 (4H, NCH_2), 109.7 (12H, N*Me*), 55.3 (4H, NCH_2), 40.1 (4H, NCH_2), 7.3 (8H, BPh_4), 7.0 (8H, BPh_4), 6.9 (4H, BPh_4), −9.4 (2H, CCH_2C), −10.2 (2H, CCH_2C). MS (+ESI): m/z 371.3 [$(M - BPh_4)^+$]. Anal. Calcd (found) for $C_{40}H_{55}BFeN_4O_2$: C, 69.57 (70.03); H, 8.03 (8.10); N, 8.11 (8.14).

Synthesis of Oxoiron(IV) Complexes. The synthesis of **3** and **4** was carried out by the addition of approximately 3 equiv of solid PhIO to acetonitrile solutions of the respective iron(II) complexes, followed by stirring at ambient temperature for 5−20 min. Subsequent removal of unreacted oxidant by filtration provided solutions of the desired complexes, suitable for spectroscopic and kinetic studies. Complexes **5** and **6** were generated by addition of 2.5−5 equiv of tetrabutylammonium acetate or propionate to solutions of $[Fe^{IV}(O)(TMC)(CH_3CN)]^{2+}$ in acetonitrile following procedures described by Jackson et al. for a series of anion-substituted $[Fe^{IV}(O)(TMC)(X)]^+$ complexes.[27]

X-ray Crystallography. Diffraction-quality crystals of [**4***][$B(C_6F_5)_4$] were grown by vapor diffusion of diethyl ether into concentrated CH_3CN solutions of the complex at ∼−35 °C in an oxygen-free environment. A crystal (approximate dimensions 0.25 × 0.21 × 0.13 mm^3) was placed onto the tip of a 0.1 mm diameter glass capillary and mounted on a Bruker CMOS diffractometer for data collection at 123(2) K.[46] A preliminary set of cell constants was calculated from reflections harvested from three sets of 20 frames. These initial sets of frames were oriented such that orthogonal wedges of reciprocal space were surveyed. This produced initial orientation matrices were determined from 782 reflections. The data collection was carried out using Cu Kα radiation (graphite monochromator) with a shutterless data collection procedure. A randomly oriented region of reciprocal space was surveyed to the extent of one sphere and to a

DOI: 10.1021/acs.inorgchem.6b02659
Inorg. Chem. 2017, 56, 3287−3301

resolution of 0.84 Å. The intensity data were corrected for absorption and decay (SADABS).[47] Final cell constants were calculated from the *xyz* centroids of 9904 strong reflections from the actual data collection after integration (SAINT).[48]

For [**5***][BPh_4], a concentrated solution in CH_3CN was layered with diethyl ether and put in a −40 °C freezer for an extended period. Selected single crystals were placed onto the top of 0.1 mm diameter glass capillaries and mounted on a Bruker SMART V5.054 CCD area detector diffractometer for data collection at 173(2) K. A preliminary set of cell constants was collected from reflections harvested from three sets of 20 frames. These initial sets of frames were oriented such that orthogonal wedges of reciprocal space were surveyed and then used to produce initial orientation matrices. Data collection was carried out using Mo Kα radiation (graphite monochromator). A randomly oriented region of reciprocal space was surveyed to the extent of one sphere, with four major sections of frames being collected using 0.30° steps in ω at four different ϕ settings and a detector position of −28° in 2θ. The intensity data were corrected for absorption and decay (SADABS).[47] Final cell constants were calculated from the actual data collection after integration (SAINT).[48]

The structures were solved and refined using Bruker SHELXTL.[49] Space groups were determined on the basis of systematic absences and intensity statistics. In all cases, a direct-methods solution was calculated, which provided most non-hydrogen atoms from the *E* map. The remaining non-hydrogen atoms were located by full-matrix least-squares/difference Fourier cycles. All non-hydrogen atoms were refined with anisotropic displacement parameters. All hydrogen atoms were placed in ideal positions and refined as riding atoms with relative isotropic displacement parameters.

Spectroscopic Experiments. Mössbauer spectra were recorded with a home-built spectrometer, using a Janis Research (Wilmington, MA) Super Varitemp Dewar. Isomer shifts are quoted relative to Fe metal at 298 K. Mössbauer samples were generated following the procedures described above but from ^{57}Fe-labeled precursors.

Resonance Raman spectra were obtained using a liquid nitrogen cooled CCD detector (Model LN/CCD-1340 × 400PB, Princeton Instruments) attached to a 1 m polychrometer (Model MC-100DG, Ritsu Oyo Kogaku). An excitation wavelength of 406.7 nm was provided by a Kr^+ laser (Spectra Physics BeamLok 2060-RM) with ca. 20 mW power at the samples. All measurements were carried out in frozen solution with samples mounted on a brass cold finger. Raman shifts were calibrated with indene, and the accuracy of the peak positions of the Raman bands was ±1 cm^{-1}. The ^{18}O-labeled isotopomers of **3** and **4** were generated by reaction with 2 equiv of $PhI(OAc)_2$, in the presence of 100 equiv of $H_2{}^{18}O$. The ^{18}O-labeled isotopomer of **5** was generated by ligand exchange from $[Fe^{IV}(^{18}O)(TMC)(CH_3CN)]^{2+}$ made using $PhI^{18}O$.

X-ray absorption spectroscopy data were collected at the Stanford Synchrotron Radiation Lightsource (SLAC National Accelerator Laboratory) on beamline 9-3 for complexes **3** and **5** and beamline 7-3 for **4**, with storage ring conditions of 3.0 GeV and 80−100 mA ring current. Fe K-edge XAS data were collected for frozen solutions maintained at a temperature of ∼15 K over an energy range of 6.9−8.0 keV using a Si(220) double-crystal monochromator for energy selection and an Oxford Instruments CF1208 continuous flow liquid helium cryostat for temperature control. Harmonic rejection was achieved using Rh-coated collimating mirrors upstream of the monochromators on both beamlines. Data were obtained as fluorescence excitation spectra with 30-element solid-state germanium detector arrays (Canberra). An iron foil spectrum was recorded concomitantly for internal energy calibration, and the first inflection point of the K-edge was assigned to 7112.0 eV. The XAS samples were prepared following procedures outlined previously (vide supra), using acetonitrile solutions of precursor complexes in concentrations ≥10 mM. Yields were quantified by electronic absorption spectroscopy, using molar extinction coefficients determined by a combination of electronic absorption and Mössbauer spectroscopic measurements.

Data reduction, averaging, and normalization were carried out with EXAFSPAK.[50] Following calibration and averaging of the data, background absorption was removed by fitting a Gaussian function to the pre-edge region and then subtracting this function from the entire spectrum. A three-segment spline with fourth-order components was then fit to the EXAFS region of the spectrum in order to extract $\chi(k)$. Analysis of the pre-edge features was carried out with the program Fityk.[51] The pre-edge feature was modeled using a Gaussian function, while the rising edge was approximated with a pseudo-Voigt. Separate fits were carried out over energy ranges of 7106−7122, 7106−7120, and 7108−7118 eV, and the reported values are the average from all three fits. EXAFS analysis was conducted with EXAFSPAK. Theoretical phase and amplitude parameters for truncated models of the relevant oxoiron(IV) complex were calculated using FEFF 8.40,[52] and relevant single and multiple scattering paths were chosen for curve fitting in the opt program of the EXAFSPAK package. In all analyses, the coordination number of a given shell was a fixed parameter and was varied iteratively while bond lengths (r) and Debye−Waller factors (σ^2) were allowed to freely float. The amplitude reduction factor S_0 was fixed at 0.9, while the edge shift parameter E_0 was allowed to float as a single value for all shells (thus in any given fit, the number of floating parameters is equal to 2 × (number of shells) + 1). Generally only single-scattering paths were considered, although we did conduct several fits for each complex that incorporate multiple scattering from the Fe−N−C_α unit of the ligand. Fits were carried out on both Fourier-filtered and unfiltered EXAFS data. We report only fits to unfiltered data, for which the goodness of fit F was defined as $[\sum k^6(\chi_{exptl} - \chi_{calc})^2/\sum k^6\chi_{exptl}{}^2]^{1/2}$.

Kinetics Experiments. Solutions of the various oxoiron(IV) complexes (0.5−1 mM) were generated as described in Synthetic Procedures and used for reactions of excess substrate at 0 °C, from which pseudo-first-order rate constants were extracted. The k_2 values were extracted from the slopes of linear plots of k_{obs} values obtained with five different concentrations of substrate. For the calculation of the Eyring parameters, all reactions were recorded at four temperatures spanning a range of 30 K. Measurements at each temperature were obtained in triplicate, and the temperature dependence was fit with the exponential form of the Eyring equation using Origin 9.1 software with $1/k_2{}^2$ weighting.

Cyclic Voltammetry. Scans were conducted at room temperature under a nitrogen atmosphere in a glovebox or in a septumed vial that had been purged with argon for 15 min. A scan rate of 100 mV/s was employed. The electrolyte was 0.1 M NBu_4PF_6. The electrodes used were glassy carbon for the working electrode, platinum wire for the auxiliary electrode, and a Ag/Ag^+ reference electrode with 0.1 M NBu_4PF_6 and 0.01 M $AgPF_6$ acetonitrile solution.

Experiments were performed using oxoiron(IV) complexes at 1 mM concentrations. **3** and **4** were generated by addition of excess iodosylbenzene to a 1 mM acetonitrile solution of iron(II) complex, as reported in Synthetic Procedures. Complexes **5** and **6** were generated by first generating $[Fe^{IV}(O)(TMC)(CH_3CN)]^{2+}$ as described above and then adding the appropriate tetraalkylammonium carboxylate salts at 3 min before scanning. The electrolyte was added prior to generation of the oxoiron(IV) complexes.

DFT Calculations. The hydrogen atom transfer reaction of all the oxoiron(IV) complexes from DHA was also studied with UB3LYP.[53,54] Since the bare complexes are positively charged, we added the counterion $CF_3SO_3^-$ to neutralize the charge and thereby avoid significant self-interaction errors.[55−57] All reactions have been studied at the UB3LYP/LACVP* (B1)[58−60] level of theory in Jaguar 8.0.[61,62] Energies were corrected subsequently using single-point calculations with the larger basis sets LACV3P+** (B2)[61,62] and Def2-TZVPP (B3).[63] To reproduce the experimental environment, higher-level corrections have been carried out in presence using the Poisson−Boltzmann solver solvation model for B2 implemented in Jaguar.[61,62] The solvent corrections have also been performed at the B3//B1 level of theory using the SMD model[64] in Gaussian 09.[65] In all cases MeCN solvation was mimicked. The charge transfer from the axial ligands to the oxidant, tunneling corrections, and kinetic isotope effect calculations have been performed. The Eckart correction was used for the determination of KIEs, as in the previous study by two of us (D.M. and S.S.).[30] Adiabatic spin state splitting energies (see Table S17 in the Supporting Information) for the 11 complexes shown in

DOI: 10.1021/acs.inorgchem.6b02659
Inorg. Chem. 2017, 56, 3287−3301

Table 2 were computed using Turbomole v7.0.1.[66−68] The B3LYP functional in combination with the def2-TZVPP basis set was used, and the COSMO[69,70] solvation model was used to mimic acetonitrile (ε = 37.5) solvation. Additional details of the computations are provided in the Supporting Information.

RESULTS AND DISCUSSION

Characterization of Iron(II) Precursors. The crystal structures of the iron(II) complexes (represented by the number associated with the oxoiron(IV) complex followed by an asterisk) [**4***][$B(C_6F_5)_4$] and [**5***][BPh_4] were solved (Figure 1), and both were found to display a five-coordinate geometry intermediate between square-based pyramidal and trigonal bipyramidal (τ[71] = 0.42 and 0.46, respectively). The iron−ligand bond lengths are typical of related high-spin iron(II) complexes.[25,28,72−76] This spin-state assignment is reinforced by the observation of well-defined paramagnetically shifted resonances in the ^{1}H NMR spectra of these complexes.

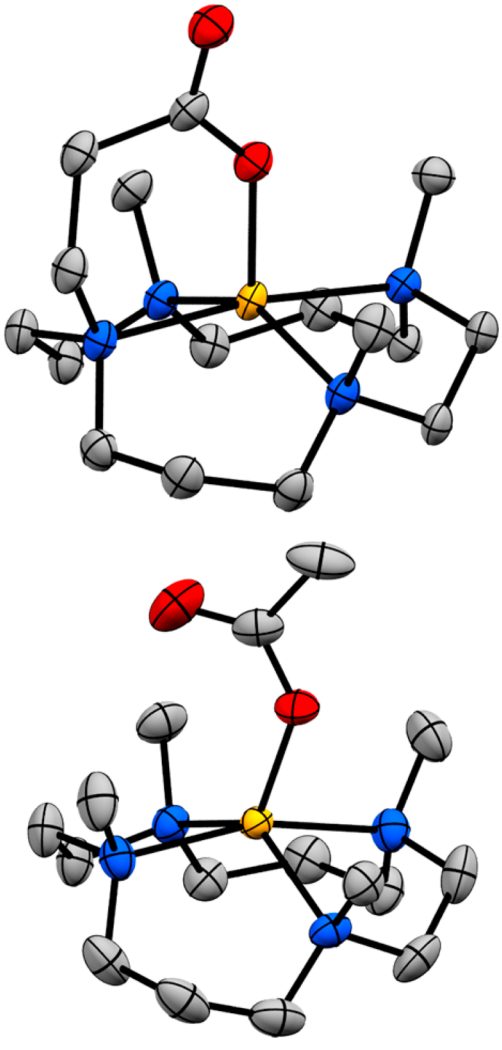

Figure 1. Crystal structures of [**4***][$B(C_6F_5)_4$] (top) and [**5***][BPh_4] (bottom) with counterions and H atoms removed for clarity. Ellipsoids are shown at the 50% probability level. Atoms are depicted as follows: carbon (gray), nitrogen (blue), oxygen (red), and iron (yellow). The structures were depicted using Mercury 3.6.[78,79] Selected bond distances for **4*** (Å): Fe−O, 1.9680(12); Fe−N_{av}, 2.20. Selected bond distances for **5*** (Å): Fe−O, 1.9310(14); Fe−N_{av}, 2.21.

(X-ray crystallography of [**3***][$B(C_6F_5)_4$] was attempted but proved unsuccessful due to the disorder resulting from the cocrystallization of enantiomers.) The macrocyclic rings of both [**4***][$B(C_6F_5)_4$] and [**5***][BPh_4] adopt a *trans*-I configuration, where all four *N*-alkyl substituents occupy one face of the macrocycle (Scheme 1 and Figure 1), in stark contrast to the *trans*-III configuration found for the Fe^{III}(TMCAc) complexes reported by Wieghardt and co-workers,[41] where two adjacent *N*-alkyl substitutents are on one face of the macrocycle opposite to the other two *N*-alkyl groups. For a detailed description of the different configurations of TMC-based complexes, see ref 77. This configurational disparity presumably derives from the five-coordinate geometry of the iron(II) complexes, which is likely a consequence of the TMC coordination cavity being unable to easily accommodate the relatively large high-spin iron(II) centers that this ligand supports. It should be noted that [**4***][$B(C_6F_5)$]$_4$ and [**5***][BPh_4] were synthesized from iron(II) precursors, while Wieghardt's Fe^{III}(TMCAc) complexes were prepared from iron(III) starting materials.

Characterization of Oxoiron(IV) Complexes. Treatment of acetonitrile solutions of iron(II) complexes **3*** and **4*** with excess iodosylbenzene elicited the formation of new species whose electronic spectra exhibit near-IR (NIR) features characteristic of S = 1 oxoiron(IV) complexes. (Figure 2 and

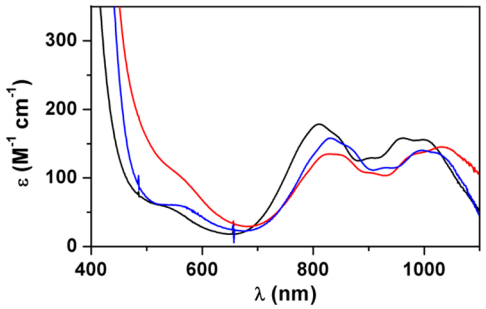

Figure 2. Near-IR region of the electronic spectra of the oxoiron(IV) carboxylate complexes **3** (black), **4** (red), and **5** (blue), obtained in CH_3CN.

Table 1). Such features have been attributed to ligand field transitions, with the associated fine structure being vibronic in nature.[80,81] Although direct oxidation of [**5***][BPh_4] with PhIO afforded [Fe^{IV}(O)(TMC)(OAc)]$^+$ (**5**), a greater yield of this complex was obtained by addition of NBu_4OAc to a MeCN solution of [Fe^{IV}(O)TMC(CH_3CN)]$^{2+}$. All spectra exhibit double-humped NIR features at ca. 800 and 1000 nm, which are typical of Fe^{IV}(O)TMC complexes with anionic axial ligands.[25,27,82] However, these bands are red-shifted from that reported by Grapperhaus et al. at 676 nm for [Fe^{IV}(O)(cyclam-acetate)]$^+$ (cyclam-acetate = 1,4,8,11-tetraazacyclotetradecane-1-acetate),[83] demonstrating the weaker field nature of the TMC ligand relative to cyclam. At 25 °C, the three TMC-based complexes exhibit drastically different thermal stabilities. Complex **3** has a half-life of 48 h, somewhat shorter than the 120 h associated with **1**, its ultrastable *N*,*N*-dimethylamide derivative[28] (Scheme 1). In contrast, **4** exhibits a half-life of 4 h, 1 order of magnitude lower than that for **3**, and **5** is even less stable with a half-life of only 3 min. These differences may be related to the flexibility of the carboxylate ligand *trans* to the oxo unit, as determined by whether the carboxylate is tethered or not and by the length of the tether when it is present, and are also reflected in the rates of substrate oxidation carried out

DOI: 10.1021/acs.inorgchem.6b02659
Inorg. Chem. 2017, 56, 3287−3301

Table 1. Spectroscopic Properties of the Oxoiron(IV) Complexes with Axial Carboxylate Ligands

complex	λ_{max} (nm) (ε_{max} (M^{-1} cm^{-1}))[a]	ν(Fe=O) (cm^{-1})	ν(C=O) (cm^{-1})	ΔE_Q (mm s^{-1})	δ_{exp} (mm s^{-1})	D (cm^{-1})	XAS pre-edge area[b]	r(Fe=O) from EXAFS (Å)
1[c]	810 (270)	833		1.10	0.13	27(2)	30	1.63
3	811 (180)	831	1682	0.74	0.13	27(2)	28	1.64
	962 (160)							
4	831 (135)	822	1645	0.82	0.17	27(2)	31	1.65
	1033 (145)							
5	831 (160)	826	1616	0.99	0.19	28.5 (20)	31	1.65
	997 (140)							
$[Fe^{IV}(O)(cyclam\text{-}acetate)]^{+}$[d]	676			1.37	0.01	23		
$[Fe^{IV}(O)(tpenaH)]^{2+}$[e]	730			0.90	0.00			

[a]Molar extinction coefficients were calculated from the near-IR absorption spectra of Mössbauer samples, from which the $Fe^{IV}O$ content could easily be measured. [b]Normalized values; see Table S2 in the Supporting Information for further details. [c]Data from ref 28. [d]Data from ref 83; other entries not available. [e]Data from ref 84; other entries not available.

by these complexes (vide infra). On the other hand, $[Fe^{IV}(O)(cyclam\text{-}acetate)]^{+}$ was much less stable; at −80 °C it was obtainable in only about 25% yield and persisted for at least 30 min to allow some spectroscopic characterization.[83] This difference in lifetime emphasizes the importance of the methyl groups in stabilizing the $Fe^{IV}(O)$ unit in the TMC-based complexes.

Complexes **3**−**5** were characterized in further detail with additional spectroscopic techniques for comparison with previously reported $Fe^{IV}(O)$TMC complexes (Table 1). They exhibited electrospray ionization mass spectra with molecular ions having m/z values and isotope distribution patterns consistent with their formulation as $[Fe^{IV}(O)(TMCAc)]^{+}$, $[Fe^{IV}(O)(TMCPr)]^{+}$, and $[Fe^{IV}(O)(TMC)(OAc)]^{+}$, respectively (Scheme 1 and Figures S1−S3 in the Supporting Information). The presence of terminal oxoiron(IV) units in **3**−**5** was confirmed by observation of ν(Fe=O) vibrations between 822 and 833 cm^{-1} in the resonance Raman spectra of these complexes obtained with 406.7 nm excitation (Figure 3 and Table 1). These features were downshifted by 32−37 cm^{-1} upon ^{18}O labeling, in good agreement with that expected for a diatomic harmonic oscillator (theoretical $\Delta\nu$ = 36−37 cm^{-1}).

Additionally, **3** and **4** exhibit ^{1}H NMR spectra containing a large number of well-resolved paramagnetically shifted resonances that are consistent with the presence of a single C_1-symmetric species in solution (Figure 4; peak assignments are provided in Figure S5 in the Supporting Information). These spectra look quite similar in pattern to that found in the ^{1}H NMR spectrum of **1**, which has been isolated as a pure crystalline solid.[28] In contrast, the ^{1}H NMR spectrum of **5** (Figure S6 in the Supporting Information) is much simpler, showing a smaller number of peaks that reflects its effective C_{2v} symmetry. For example, the four *N*-methyl groups of **5** appear as a single peak at −49.4 ppm, while the *N*-methyl groups of **3** and **4** become resolved into two or three peaks in the same region because of their C_1 symmetry. No features arising from their iron(II) precursors (see the Experimental Section for a listing of the NMR signals of **3***, **4***, and **5***) were discernible, suggesting complete oxidation of the precursors, which was also confirmed by the high yields of $Fe^{IV}(O)$ complexes observed in

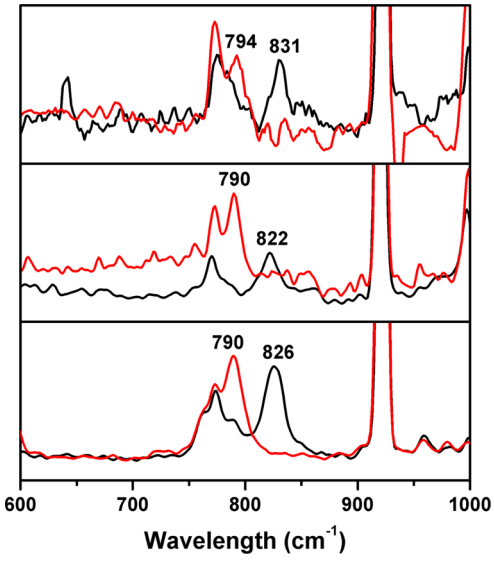

Figure 3. Resonance Raman spectra (λ_{ex} 406.7 nm, power 20 mW) of the oxoiron(IV) complexes (black lines) and their ^{18}O-labeled isotopomers (red lines), recorded in frozen CH_3CN solution: (top) **3**; (middle) **4**; (bottom) **5**.

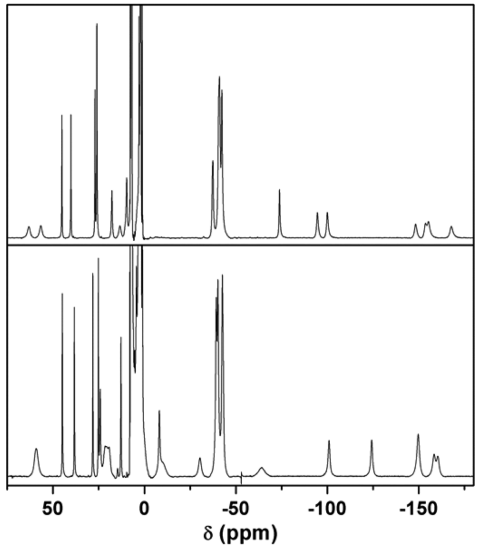

Figure 4. ^{1}H NMR spectra of **3** (top) and **4** (bottom) recorded in CD_3CN solution at room temperature. Conditions: acquisition time 0.064 s; relaxation delay 0.03 s; line broadening factor 30 Hz. Peak assignments are provided in Figure S5 in the Supporting Information.

DOI: 10.1021/acs.inorgchem.6b02659
Inorg. Chem. 2017, 56, 3287−3301

their Mössbauer spectra (vide infra). Contributions from iron(III) species (if present) are not observed, but they would not be expected to be seen because of their much broader linewidths arising from unfavorable electronic spin relaxation times.

Mössbauer studies on **3**−**5** corroborate their expected $S = 1$ spin state. Zero-field spectra recorded at 4.2 K exhibit dominant (>90% of total) Fe quadrupole doublets with quadrupole splittings, ΔE_Q, of 0.74−0.99 mm/s and isomer shifts, δ, of 0.13−0.19 mm/s (Table 1 and Figure S7 in the Supporting Information). Applied magnetic fields, B, elicit magnetic hyperfine interactions with parameters typical of $S = 1$ Fe^{IV}═O complexes (Figures S8−S12 and Table S1 in the Supporting Information), which have been analyzed using the $S = 1$ spin Hamiltonian

$$\mathcal{H}_e = D(\hat{S}_z^2 - 2/3) + E(\hat{S}_x^2 - \hat{S}_y^2) + \beta\hat{S}\cdot\mathbf{g}\cdot\mathbf{B} + \hat{S}\cdot\mathbf{A}\cdot\hat{I} - g_n\beta_n\mathbf{B}\cdot\hat{I} + \mathcal{H}_Q$$

$$\mathcal{H}_Q = eQV_{zz}/12[3\hat{I}_z^2 - 15/14 + \eta(\hat{I}_x^2 - \hat{I}_y^2)] \quad (1)$$

where all symbols have their conventional meanings (see the Suppporting Information). Within resolution, the zero-field splitting (ZFS) tensor, described by the parameters D and E, was found to be axial ($E = 0$). D was obtained by fitting variable-field/variable-temperature spectra recorded between 4.2 and 100 K (Figures S8−S12 in the Supporting Information), and the D values obtained were typical of other [Fe^{IV}(O)(TMC)] complexes.[27] In the Supporting Information we also comment on the Fermi contact contribution to the ^{57}Fe magnetic hyperfine tensor. It is interesting to note the resemblance of the isomer shift and D values for **1** and **3** with only the quadrupole splitting, reflecting the difference in the charge of the axial ligand. In contrast to the TMC-based complexes, [Fe^{IV}(O)(cyclam-acetate)]$^+$ exhibits a much smaller isomer shift and a smaller D value (Table 1), emphasizing the stronger field nature of the cyclam macrocycle versus TMC.

In order to gain structural information for the carboxylate-bound oxoiron(IV) complexes, we have obtained XAS data for **3**−**5**. The XANES region exhibit spectra of similar shape and intensity, which suggests that the iron centers all have similar structural and electronic environments (Figure 5 top). The edge energies are typical of previously reported $S = 1$ oxoiron(IV) complexes. In **3**−**5**, a single intense pre-edge feature is observed at ca. 7114 eV, arising from 1s → 3d transitions that gain intensity from 3d−4p orbital mixing, the extent of which is dictated by the degree of distortion away from centrosymmetry at the iron center. In contrast to the previously reported series of anion-bound oxoiron(IV) complexes of TMC, there are only slight variations in the area of the pre-edge feature. Given the magnitude of experimental error, we have not attempted to correlate these data with other spectroscopic properties.

The $k^3\chi(k)$ EXAFS spectra of all three oxoiron(IV) complexes are very similar, with comparable oscillations and EXAFS amplitudes for values of $k < 10$ Å^{-1} (Figure 5 bottom). The dampening of oscillations for $k > 10$ Å^{-1} is almost complete. As might be expected, the Fourier transforms of the EXAFS spectra are also fairly similar and are best fit with a single O/N scatterer at 1.63 Å and a shell of four to five O/N scatterers at 2.03−2.07 Å that can be attributed to the Fe═O unit and donors of the supporting ligand, respectively (Tables

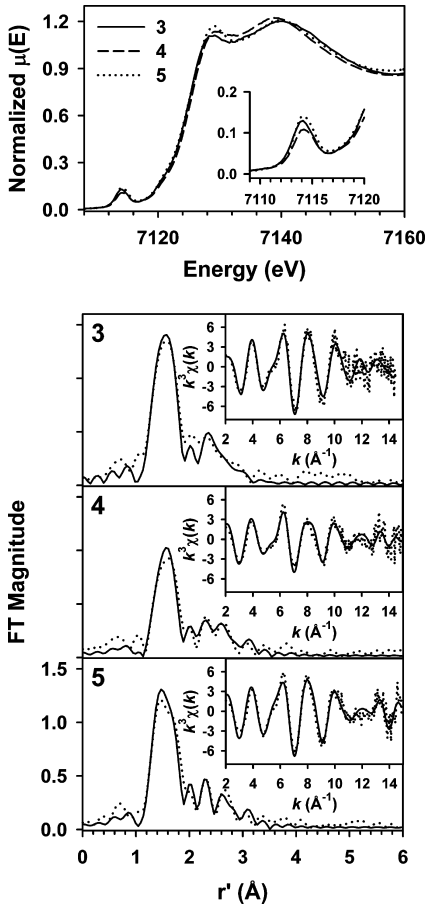

Figure 5. (top) Comparison of the Fe K-edge X-ray absorption edge and pre-edge (inset) features of **3** (—), **4** (- - -), and **5** (···). (bottom) Fits to the Fourier transforms of the Fe K-edge EXAFS data ($k^3\chi(k)$) and either Fourier-filtered or unfiltered EXAFS spectra ($k^3\chi(k)$, insets) for **3**−**5**. Experimental data are shown with dotted lines (···), while fits are shown with solid lines (—). Fit parameters are given in bold italics in Tables S3−S5 in the Supporting Information.

S3−S5 in the Supporting Information). Addition of the Fe═O scatterer resulted in profound improvements to the quality of the fit, suggesting that in all cases it constituted an integral component of the EXAFS modulations. Furthermore, it was found that splitting the primary shell of O/N scatterers into two subshells, corresponding to equatorial and axial donors, resulted in either chemically unreasonable bond lengths and Debye−Waller factors for the latter scatterer or differences between the Fe−$N_{equatorial}$ and Fe−N/O_{axial} distances smaller than the resolution limit of the available data (0.12−0.13 Å). Given that the Fe═O distances are identical in all the complexes and the variation of 0.04 Å in the primary shell of O/N scatterers is within the error of the experiment (±0.02 Å for metal−ligand bond lengths), it can be concluded that all three oxoiron(IV) complexes exhibit near-identical first shell coordination parameters, emphasizing the similar structural features of these compounds.

Zero-field Mössbauer studies show that **3**−**5** exhibit quadrupole doublets having isomer shifts δ typical of Fe^{IV}(O)TMC complexes. Fitting of the high-field spectra of these complexes provided zero-field splitting and hyperfine parameters similar to those of previously reported $S = 1$ oxoiron(IV) complexes. More specifically, the zero-field spectrum of **3** displayed a doublet with $\delta = 0.13$ mm s^{-1} and

DOI: 10.1021/acs.inorgchem.6b02659
Inorg. Chem. 2017, 56, 3287−3301

ΔE_Q = 0.74 mm s^{-1}, typical of anion-bound oxoiron(IV) complexes with TMC-based ligands. Notably, an increase was observed in both δ and ΔE_Q upon increasing the length of the pendant donor arm to the propionate-appended complex **4** (δ = 0.17 mm s^{-1} and ΔE_Q = 0.82 mm s^{-1}) and moving to the unappended acetate complex **5** (δ = 0.19 mm s^{-1} and ΔE_Q = 0.99 mm s^{-1}). Given that the magnitude of ΔE_Q can crudely be viewed as a reflection of the degree of asymmetry in the electron density around the iron center and δ is inversely related to the electron density at the iron nucleus, the smaller ΔE_Q and δ values seen in **3** are in part a reflection of the slightly greater donor strength of the appended acetate, relative to the other carboxylate-bound complexes **4** and **5**. This is presumably a consequence of the small five-membered chelate ring formed by coordination of the appended acetate in **3** and any conformational changes in the cyclam ring derived therefrom.

Though there is little obvious correlation between the Mössbauer parameters observed for the carboxylate complexes $[Fe^{IV}(O)(L)]^+$ and their ν(Fe=O) values, the carboxylate C=O stretching frequencies ν(C=O) (Figure 6, where **3** > **4** > **5**)

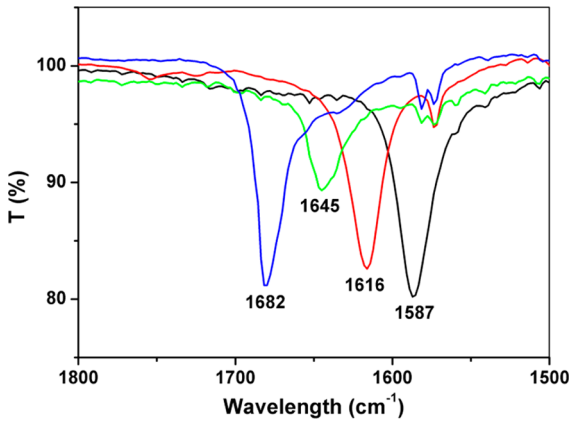

Figure 6. IR spectra of $[Fe^{IV}(O)L]^+$ complexes **3** (blue line), **4** (green line), and **5** (red line) in CH_3CN solution at ambient temperature. For reference, a spectrum of NBu_4OAc (black line) is included. Corresponding spectra for the iron(II) precursors are shown in Figure S13 in the Supporting Information.

were found to increase with decreasing ΔE_Q. The increasing ν(C=O) value reflects a greater localization of the carboxylate negative charge on the O atom bound to the iron, suggesting the strengthening of the Fe–$O_{carboxylate}$ bond that is in turn indicated by the decrease in the Mössbauer quadrupole splittings (**3** < **4** < **5**, Table 1). As might be expected, the ν(C=O) values in these complexes were observed at frequencies higher than that of $Bu_4N(OAc)$, in which the accompanying anionic charge is presumably fully delocalized over the carboxylate moiety. (A similar increasing trend was found for the ν(C=O) values of the corresponding iron(II) precursors of **3**–**5** (Figure S13 in the Supporting Information).)

Reactivity Comparisons. As described in the Introduction, the HAT reactivity of a series of TMC-based oxoiron(IV) complexes has been found to increase with the basicity of the axial ligand *trans* to the oxo unit. This antielectrophilic pattern was first rationalized within the framework of a two-state reactivity (TSR) model,[26,28] but subsequent work has suggested that the HAT reactivity of TMC-based oxoiron(IV) complexes may be more complicated.[26,28] We thus set out to investigate how changing structural components of the TMC framework affects the reactivity with a series of axially bound carboxylate complexes.

As in previous studies of $[Fe^{IV}(O)(TMC)(X)]^{n+}$ complexes,[26] the $E_{p,c}$ values (obtained by cyclic voltammetry, Figures S15–S18 in the Supporting Information) of the oxoiron(IV) complexes described herein have been selected as a measure of the electrophilicity of their $Fe^{IV}(O)$ units. Included in the reactivity study with complexes **3**–**5** described earlier is $[Fe^{IV}(O)(TMC)(O_2CCH_2CH_3)]^+$ (**6**) as an untethered analogue of **4**. Complex **6** was generated by addition of approximately 3 equiv of $Bu_4N(O_2CCH_2CH_3)$ to $[Fe^{IV}(O)(TMC)(NCCH_3)]^{2+}$ in acetonitrile solution, which gave rise to near-IR bands at 837 and 1030 nm, similar to those of **5**, and an ESIMS spectrum with a peak at m/z 401.2 having an isotope distribution pattern corresponding to $[Fe(O)(TMC)(O_2CCH_2CH_3)]^+$ (Figure S4 in the Supporting Information). Perhaps not surprisingly, the $E_{p,c}$ values associated with **3**–**6** span only a range of 130 mV (Table 2), with the appended acetate complex having the lowest value of −920 mV vs Fc^+/Fc and the untethered acetate complex having the highest value at −790 mV vs Fc^+/Fc. However, the oxygen atom transfer (OAT) rates to PPh_3 within the carboxylate series show a difference of 2 orders of magnitude (Table 2). The appended acetate complex **3** is the least reactive with a k_2 value of 0.006 M^{-1} s^{-1}, followed by the appended propionate complex **4** with a 10-fold higher k_2 value of 0.071 M^{-1} s^{-1}, while the untethered carboxylate complexes **5** and **6** exhibit comparable k_2 values that are yet another 10-fold higher. As shown in Figure 7, the logarithms of the measured second-order rate constants for the four carboxylate complexes versus their $E_{p,c}$ values show a proportional increase in reactivity with redox potential (Table 2).

Interestingly, the reactivity patterns for CHD and DHA oxidation by the four carboxylate complexes mirror that for PPh_3 oxidation, with the plots of log k_2 versus $E_{p,c}$ for all three substrates affording approximately parallel lines, with the complex having a more positive potential being a more reactive oxidant in HAT reactions. This trend is also reflected in the Eyring parameters obtained for CHD oxidation by all four carboxylate complexes, where the tethered carboxylate complexes exhibit higher enthalpies of activation (43(2) kJ/mol for **3** and 39(2) kJ/mol for **4**) than the untethered carboxylate complexes (32(2) kJ/mol for **5** and 34(2) kJ/mol for **6**) (Table 2). On the other hand, the entropies of activation range from −108(7) to −119(6) J/(mol K) and are essentially within error identical for all four carboxylate complexes (Table 2). The difference seen between the HAT reactivities of the tethered and untethered carboxylate complexes is, therefore, due to enthalpic differences. For all four carboxylate complexes, KIE values for DHA oxidation were found to fall between 15 and 20, which are comparable to those previously reported for **7** and **8** (Table 2); these nonclassical values are ascribed to a tunneling contribution.[26]

Figure 8 compares the reactivity properties of the carboxylate series within the greater context of other $[Fe^{IV}(O)(TMC)(X)]$ complexes. Figure 8A shows OAT rates to PPh_3 plotted versus their experimentally determined $E_{p,c}$ values, where the rates of the carboxylate complexes (red circles) fall reasonably on the line defined by the black squares representing the original four entries in the $[Fe^{IV}(O)(TMC)(X)]$ series described by Sastri et al., where X = MeCN (**10**), O_2CCF_3 (**8**), N_3 (**7**), SR (**11**) (from right to left).[26] Additional entries include data for

DOI: 10.1021/acs.inorgchem.6b02659
Inorg. Chem. 2017, 56, 3287–3301

Table 2. Reactivity of [Fe^{IV}(O)(TMC)(X)] Complexes in MeCN at 0 °C

complex	$t_{1/2}$(25 °C)	k_2 (M^{-1} s^{-1}) PPh$_3$	CHD	DHA[a]	KIE DHA	$\Delta H^{\ddagger}$[b] (kJ/mol)	$\Delta S^{\ddagger}$[b] (J mol^{-1} K^{-1})	$E_{p,c}$(25 °C) (V vs Fc)
3	48 h	0.0057(4)	0.023(1)	0.033(4) [2.5 × 10^{-3}][c]	~15[c]	43 ± 2	−119 ± 6	−0.92
4	4 h	0.070(2)	0.33(6)	0.66(4) [0.032(3)]	20	39 ± 2	−108 ± 7	−0.84
5	~3 min	0.57(1)	3.6(2)	6.4(4) [0.33(1)]	19	32 ± 2	−115 ± 6	−0.79
6	~3 min	0.64(2)	4.3(2)	7.4(1) [0.44(2)]	17	34 ± 2	−108 ± 5	−0.81
[Fe^{IV}(O)(TMCdma)]$^{2+}$ (**1**)	120 h[d]	0.19[d]	0.037[d]					−0.63[d]
[Fe^{IV}(O)(TMCdma)-H]$^{+}$ (**2**)	~1.5 h (0 °C)[d]	<0.004[d,e]	0.016[d]					−1.16[d]
[Fe^{IV}(O)(TMC)(N$_3$)]$^{+}$ (**7**)	15 min[f]	0.61[i]	1.4[i]	2.4[i]	17[i]			−0.60[i]
[Fe^{IV}(O)(TMC)(O$_2$CCF$_3$)]$^{+}$ (**8**)	1 h[g]	2.9[i]	1.2[i]	1.3[i]	19[i]			−0.50[i]
[Fe^{IV}(O)(TMCpy)]$^{2+}$ (**9**)	7 h[h]	3.8[d]	0.22[d]					−0.48[d]
[Fe^{IV}(O)(TMC)(NCMe)]$^{2+}$ (**10**)	10 h[g]	5.9[i]	0.12[i]	0.14[i]	10 (25 °C)[h]			−0.32[i]
[Fe^{IV}(O)(TMCS)]$^{+}$ (**11**) in 1:1 MeCN/MeOH	5 min[f]	0.016[i]		7.5[i]				−1.0 (- 30 °C)[i]

[a]Values given in square are k_2 values for the corresponding reactions with DHA-d_4. [b]Eyring parameters for CHD oxidation. [c]Estimate based on the reaction of **3** with 100 equiv of DHA-d_4. [d]From ref 28. [e]Estimated rate due to competing self-decay. [f]From ref 27. [g]From ref 82. [h]From ref 74. [i]From ref 26.

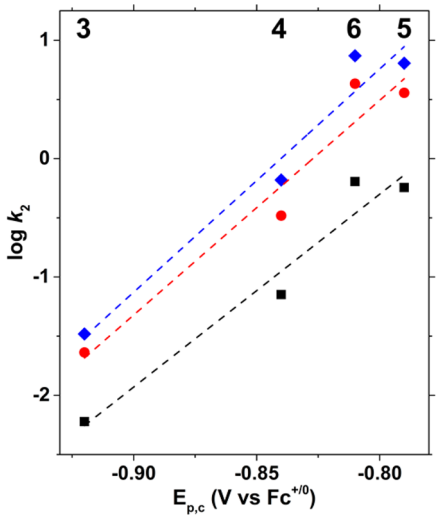

Figure 7. Plots of the logarithms of the second-order rate constants of the [Fe^{IV}(O)(TMC)(carboxylate)] complexes for the oxidation of 9,10-dihydroanthracene (blue diamonds), 1,4-cyclohexadiene (red circles), and PPh$_3$ (black squares) at 0 °C versus corresponding $E_{p,c}$ values of the complexes, obtained at 25 °C in acetonitrile.

complexes **1**, **2**, and **9**, represented by blue diamonds. This correlation demonstrates that OAT rates reflect the electrophilicity of the Fe^{IV}(O) unit, as indicated by its $E_{p,c}$ value. A similar correlation between OAT rates and redox potential has also been observed for five oxoiron(IV) complexes bearing pentadentate aminopyridine ligands.[85]

In contrast, plotting the DHA oxidation rates of the [Fe^{IV}(O)(TMC)(X)] complexes versus their $E_{p,c}$ values shows no obvious pattern (Figure 8B). The dotted black line is that associated with the four entries in the original Sastri series (black squares representing X = MeCN (**10**), O$_2$CCF$_3$ (**8**), N$_3$ (**7**), SR (**11**) from right to left).[26] Because this line has a slope which is opposite in sign relative to that for the corresponding OAT plot in Figure 8A, Sastri et al. have described this trend as antielectrophilic, and HAT rates increased with a rise in the electron-donating ability of the axial ligand. Of the other complexes added to this original plot, **5** and **6**, respective complexes with untethered acetate and propionate, fall on this line and exhibit HAT rates comparable to that of **11**, the most reactive complex in the series. However, complexes with tethered carboxylates (**3** and **4**) and tethered amides (**1** and **2**) exhibit HAT rates 1−3 orders of magnitude smaller than those predicted by this line, prompting us to look for a different factor that can rationalize the HAT reactivity observed for these complexes. This factor turns out to be the triplet−quintet spin-state gap as calculated by DFT, which will be discussed in the following section.

DFT Studies of Reactivity. Density functional theory calculations have proven useful as a tool to aid us in understanding the electronic structures of nonheme oxoiron(IV) complexes and to provide insight into the factors that affect their experimentally determined reactivity properties. For this work, we have focused on understanding the HAT reactivity trends for 11 complexes of the Fe^{IV}(O)TMC(X) series. As shown in Figure 8D, a nice correlation was obtained by plotting the logarithms of the second-order constants for HAT versus the spin-state splitting energies of the various oxoiron(IV) complexes as calculated by DFT. HAT reactivity increased as the S = 2 spin state became more accessible, thereby supporting the TSR model of Shaik.

Further calculations were carried out to predict the barriers for HAT. The computed barriers for complexes **3**−**6** reveal a reasonably matching trend with the experimental free energies of activation. This is true for either the electronic barriers corrected by solvation and zero-point energies (see Table S10 in the Supporting Information) or the corresponding free energies of activation ($\Delta G^{\ddagger}$), as well as those corrected for tunneling ($\Delta G^{\ddagger}_{eff}$).[30] Figure 9 shows the plots of the theoretical vs the experimental values. The trends in both plots are clearly identical and are in agreement with experimental trends. The experimental barriers for **5** and **6** are within 0.1 kcal/mol, while the theoretical barriers are within 0.6−0.9 kcal/mol. These variations are within the error margins of both experiment and theory.

As can be seen from Figure 9, the theoretical $\Delta G^{\ddagger}$ values are higher than the tunneling corrected values, $\Delta G^{\ddagger}_{eff}$, by roughly a

DOI: 10.1021/acs.inorgchem.6b02659
Inorg. Chem. 2017, 56, 3287−3301

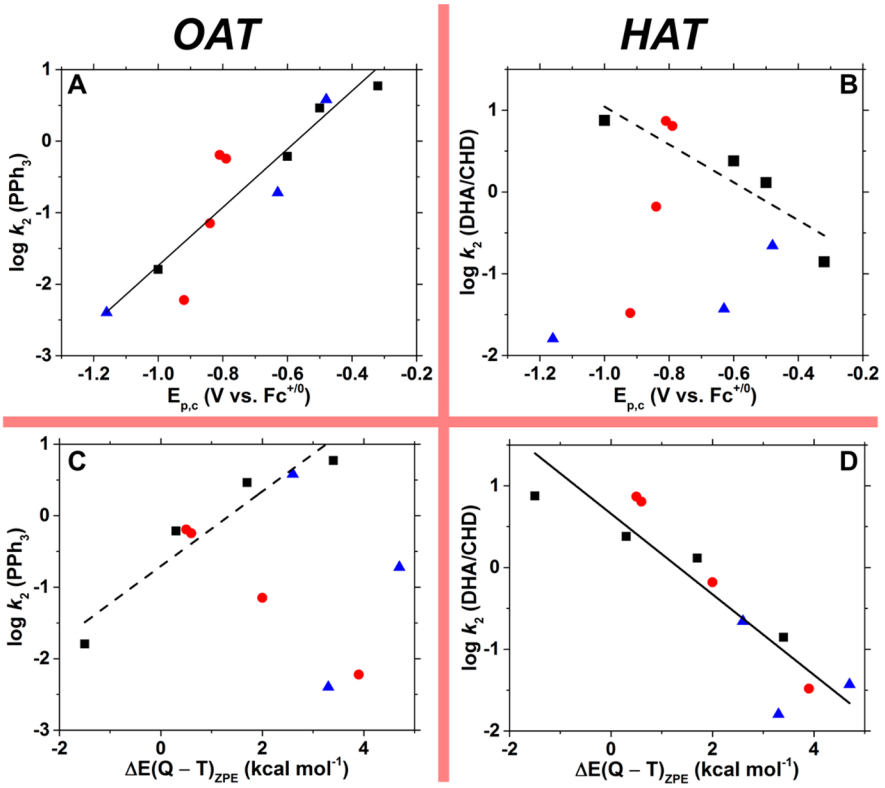

Figure 8. Logarithms of the oxidation rate constants for TMC-based oxoiron(IV) complexes at 0 °C versus the reductive peak potential from cyclic voltammetry (top row) and the computed spin state splitting energy difference between the ground triplet and the excited quintet states (bottom row). Panel A shows OAT data with PPh_3 as substrate, where red circles represent the carboxylate complexes **3**–**6**, black squares represent [Fe^{IV}(O)(TMC)(X)] complexes in the original series reported by Sastri et al. in ref 26 where X = MeCN, O_2CCF_3, N_3, SR, and blue triangles correspond to **1**, **2**, and **9** reported by England et al. in ref 28 (see Table 2 for actual values). Panel B plots HAT data for the same set of complexes; red circles and black squares represent DHA oxidation rates, and blue triangles correspond to CHD oxidation rates. Panels C and D respectively show plots of the logarithms of the OAT and HAT rates versus the computed spin state splitting energies. Good correlations for all data were obtained in panels A and D. The black dotted lines in the plots in panels B and C correspond to the fits to the data represented by the black squares reported in ref 26.

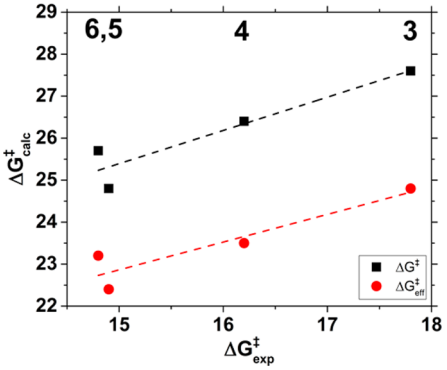

Figure 9. Calculated activation free energies ($\Delta G^{\ddagger}$) and effective free energies of activation ($\Delta G^{\ddagger}_{eff}$) (at the B3 level at 273 K) vs experimental barriers of activation ($\Delta G^{\ddagger}_{exp}$ based on second-order rate constants k_2) for the HAT reactions of **3**–**6** with DHA. All values are given in kcal mol^{-1}.

constant shift. Tunneling contributions were introduced into our calculations, as was noted by two of us (D.M. and S.S.)[30] that an increased tunneling contribution for complexes with more electron donating *trans* ligands could give rise to the antielectrophilic trend observed in the original work of Sastri et al.[26] and the larger KIEs found for the more reactive complexes in that subset. Our observation of a constant tunneling contribution in the present study indicates that the tunneling correction to the barrier is not highly variable for complexes **3**–**6**, which is consistent with the experimentally observed trends. We do note that the trends are reproduced well, while the free energies of activation are systematically overestimated by ∼10 kcal mol^{-1}. Such a behavior was also observed previously for oxoiron(IV) complexes with TMC ligands.[30] Table 3 collects the tunneling corrections of the barriers, the values of the imaginary frequencies in the TSs, the amounts of charge transferred from the axial ligand to the rest of the oxidant (Δq_{CT}), and the theoretical and experimental KIE values. It is apparent that the tunneling-corrected theoretical KIE values for **3**–**6**, ranging from 30 to 39 for the quintet state (S = 2) reactivity (the semiclassical Eyring KIE values being 5.3–8.0; see Table S9 in the Supporting Information) are higher than the experimental values but are of the same order of magnitude. Therefore, we also calculated the KIEs of the complexes with trifluoroacetate and azide ligands and found them to be much closer to experiment. We cannot explain why the calculated KIE values are somewhat overestimated for **3**–**6**. Nevertheless, an important mechanistic conclusion can be drawn from the data in the table regarding the role of KIE as a probe of the reactive spin state. As the KIEs calculated for the triplet state, S = 1, path are between 1 and 2 orders of magnitude higher than the experimental data, only the calculated KIE values for S = 2 match the experimental values in magnitude and trend. As such,

DOI: 10.1021/acs.inorgchem.6b02659
Inorg. Chem. 2017, 56, 3287–3301

Table 3. Charge Transfer, Δq_{CT}, from the Axial Ligand, Imaginary Frequency, $\nu_H^{\ddagger}$, Tunneling Contribution, $\Delta(\Delta G^{\ddagger}-\Delta G^{\ddagger}_{eff})$, and the Calculated and Experimental Kinetic Isotope Effects, KIE (273 K), for the Reaction of $[Fe^{IV}(O)L]$ Complex with DHA at the $S = 2$ Surface

oxidant	$\Delta(\Delta G^{\ddagger}-\Delta G^{\ddagger}_{eff})$	$\nu_H^{\ddagger}$ ($S = 2$)	Δq_{CT} [a]	KIE_{cal}		KIE_{expt}
				$S = 1$	$S = 2$	
3	2.8	1715	−0.480	475	38	**15**
4	2.9	1740	−0.496	538	39	**20**
5	2.4	1634	−0.219	1110	30	**19**
6	2.5	1624	−0.220	1195	37	**17**
$[Fe^{IV}(O)(TMC)(O_2CCF_3)]^-$	1.9	1480	−0.185	1045	16	**19** [b]
$[Fe^{IV}(O)(TMC)(N_3)]^-$	2.4	1614	−0.290	[c]	22	**17** [b]

[a]Calculated using natural population analysis. [b]See ref 26. [c]Not available for the $S = 1$ spin state.

the KIE values identify the $S = 2$ state as the reactive state and support once more the TSR notion.[32−34]

Although our calculations on the reactivity of complexes **3**−**6** are consistent with the experimental observations and show that the reactivity of the oxoiron(IV) complexes of the TMC family does not necessarily have to follow an antielectrophilic trend, they do not rationalize the origin of the large difference in reactivity of the complexes studied here. One might speculate that the geometrical distortions on approaching the transition state are influenced by appending the carboxylate ligand in this series of complexes. To check this effect, we have first inspected the geometries of the transition states, which are depicted in Figure S21 in the Supporting Information, and found that the structures are almost alike and reveal no special gas-phase distortions that distinguish the complexes with appended ligands from those with unappendend ligands. We therefore proceeded to calculate the corresponding distortion/deformation energies for the reactants in the ^{5}TS species relative to the relaxed reactants in the $S = 1$ ground states. The results are shown in Table 4. For references regarding the development of the method, see refs 86 and 87. For the use of the term distortion energy, see refs 88 and 89. For the use of the terms distortion/deformation energies, see refs 90−95. For a similar development and use of the term "activation strain", see refs 96 and 97.

Table 4. Computed Solvent-Phase Relative Distortion Energies (ΔE_{dis}), Electronic Barriers ($\Delta E^{\ddagger}$), and Experimental Free Energy Barriers for the HAT Reactions of **3**−**6** with DHA

level of theory	oxidant	ΔE_{dis} [a] (substrate)	ΔE_{dis} [a] (oxidant $S = 1$)	ΔE_{dis} [a] (total)	$\Delta E^{\ddagger}$ ($S = 1 \rightarrow S = 2$) [b]	$\Delta G^{\ddagger}_{273\,K}$ (exp)
B2-Solv (PBS)	**3**	10.4	8.6	19.0	20.7	17.8
	4	10.6	7.8	18.4	18.0	16.2
	5	9.8	6.7	16.5	16.2	14.9
	6	9.8	6.9	16.7	16.9	14.8
B3-Solv (SMD)	**3**	10.3	8.6	18.9	22.0	17.8
	4	10.6	7.5	18.1	20.2	16.2
	5	9.8	7.1	16.9	18.8	14.9
	6	9.8	7.3	17.1	19.2	14.8

[a]These quantities correspond to the distortion energies (or barriers) from the $S = 1$ ground state to the transition state at $S = 2$. For the oxidant, the ΔE_{dis} quantity involves the energy difference of the deformed quintet oxidant moiety in the TS geometry and the relaxed ground-state oxidant. [b]These are the electronic energy barriers (no ZPE corrections).

Table 4 shows only data obtained in combination with a continuum solvation model (see also Tables S11 and S13 in the Supporting Information for complete data). The reactivity is mainly controlled by the distortion energy from ground $S = 1$ to corresponding TSs on the $S = 2$ states. If we separate this factor into two terms, e.g. $S = 1$ reactant to $S = 2$ reactant and then $S = 2$ reactant to $S = 2$ TS, it is found that the distortion energy for the $S = 2$ reactant to the $S = 2$ TS is almost constant for all of the oxidants (see Table S13). Thus, the spin state energy differences, $\Delta E(Q-T)_{ZPE}$, make the major contribution to the reactivity differences, and this factor is automatically included in the aforementioned distortion energy from the $S = 1$ to the $S = 2$ pathway. After incorporating solvent effects, we find that the distortion energies, including corrections from the solvation models, are in better agreement with experiment. In the gas phase **4** shows a distortion energy almost similar to that of **5**, even though **4** is substantially less reactive than **5**. However, including solvation raises the distortion energies and barriers of **4** and improves the trends. It appears therefore that the distortion energy and solvation effects control the experimentally observed trends.

We further clarify the correlation between $\Delta E(Q-T)_{ZPE}$ and the log of the second-order rate constants for HAT reactions upon recalculation of the spin state splitting energies $\Delta E(Q-T)_{ZPE}$ for the 11 complexes shown in Table 2 using a common protocol (B3LYP/def2-TZVPP in combination with the COSMO solvation model for MeCN; see the Supporting Information for additional details). The nice correlation between log k_2 for HAT by these complexes versus $\Delta E(Q-T)_{ZPE}$ is shown in Figure 8D, further manifesting the importance of the accessibility of the $S = 2$ spin state in order to promote efficient reactivity within a TSR scenario. Notably, it also shows no sensitivity to the experimentally determined KIE values.

In stark contrast to the HAT data, the log k_2 values for the OAT reactions correlate only with $E_{p,c}$ (Figure 8A) and not with $\Delta E(Q-T)_{ZPE}$ (Figure 8C). The differences between HAT and OAT have been previously treated using the valence bond (VB) model of reactivity,[98,99] where it was demonstrated that the major factor in OAT is the interaction of the reactant state with the charge-transfer state, but this interaction is only secondary in HAT. Indeed, the present correlations clearly indicate different activation scenarios for OAT and HAT. In previous computational studies, OAT for oxoiron(IV) complexes with an $S = 1$ ground state has also been attributed to a TSR scenario,[30,31,100−102] which in light of the present results warrants reinvestigation using VB modeling of the two reactivity scenarios.

DOI: 10.1021/acs.inorgchem.6b02659
Inorg. Chem. 2017, 56, 3287−3301

CONCLUSION

We have synthesized and characterized a series of oxoiron(IV) complexes supported by the TMC macrocycle to assess the effect of introducing an axially coordinated carboxylate ligand on the spectroscopic and reactivity properties of the oxoiron(IV) moiety. Two pairs of complexes have been investigated: one pair having axial acetate and propionate ligands and the other pair having these carboxylates tethered to the TMC ligand by replacement of one of its methyl groups. While carboxylate tethering has a measurable but not that great of an effect on the spectroscopic properties of the oxoiron(IV) complexes, OAT and HAT rates of the untethered complexes **5** and **6** are 10−100-fold faster than those of the tethered complexes **3** and **4**. An Eyring analysis of CHD oxidation by the four carboxylate complexes reveals that the differences in HAT reactivity can be attributed to a change in activation enthalpy, where complexes bearing untethered carboxylate ligands show lower values, in agreement with their higher reactivity. When this set of data is viewed within the context of 11 characterized oxoiron(IV) complexes of the TMC family (Table 2), it is found that OAT rates correlate linearly with experimentally measured $E_{p,c}$ values (Figure 8A), in agreement with the electrophilic trend first noted by Sastri et al. for a subset of four complexes.[26] However, the corresponding antielectrophilic trend for HAT rates observed for this original subset does not hold up for the entire family, particularly for the complexes with tethered carboxylates and amides (Figure 8B). Furthermore, tunneling contributions do not appear to be a factor. Although tunneling is clearly involved in the HAT reactions on the basis of the nonclassical values measured, the values for **3**−**6** fall into the same narrow range (15−20) as found for **7** and **8**. On the other hand, the HAT rates for the 11 complexes in this family correlate with calculated triplet−quintet spin state splitting energies ($\Delta E(Q-T)_{ZPE}$) (Figure 8D), as observed for the original subset of complexes, thereby ascertaining that the TSR model applies generally to complexes within the TMC family. In contrast, the OAT rates do not show a correlation with $\Delta E(Q-T)_{ZPE}$ (Figure 8C), as the complexes having tethered carboxylates and amides, namely **1**−**4**, are the outliers in this plot. These results thus highlight differences in which factors control OAT and HAT reactivity in synthetic model complexes of nonheme oxoiron(IV) complexes. These findings become particularly relevant with the recent demonstration that OAT-type reactivity occurs at the oxoiron(IV) site of a new nonheme iron enzyme: namely, the epoxidase AsqJ.[103]

ASSOCIATED CONTENT

Supporting Information

The Supporting Information is available free of charge on the ACS Publications website at DOI: 10.1021/acs.inorgchem.6b02659.

Crystallographic and structure refinement data for [**4***][$B(C_6F_5)_4$] and [**5***][BPh_4], spectroscopic data for oxoiron(IV) complexes **3**−**6**, IR data for **3***−**5***, cyclic voltammetric data for **3**−**6**, and full computational details and Cartesian coordinates (PDF)

Crystallographic data (CIF)

Crystallographic data (CIF)

AUTHOR INFORMATION

Corresponding Authors

*E-mail for E.M.: emunck@andrew.cmu.edu .

*E-mail for S.S.: sason@yfaat.ch.huji.ac.il.

*E-mail for L.Q.: larryque@umn.edu.

ORCID

Sason Shaik: 0000-0001-7643-9421

Lawrence Que Jr.: 0000-0002-0989-2813

Present Address

[‖]J.E.: Division of Chemistry and Biological Chemistry, School of Physical and Mathematical Sciences, Nanyang Technological University, 21 Nanyang Link, Singapore 637371. E.R.F.: Case Western Reserve University Center for Synchrotron Biosciences and Center for Proteomics and Bioinformatics, National Synchrotron Light Source II, Brookhaven National Laboratory, Upton, NY 11973, United States. J.R.F.: Department of Chemistry and Physics, University of Wisconsin—Stout, Menomonie, WI 54751, United States. M.M.: Aix Marseille University, CNRS, BIP UMR 7281, Marseille, France.

Notes

The authors declare no competing financial interest.

ACKNOWLEDGMENTS

This work was supported by grants from the U.S. National Science Foundation (CHE-1361773 to L.Q. and CHE-1305111 to E.M.) and a Feodor Lynen Research Fellowship from the Alexander von Humboldt Foundation to J.E.M.N.K. S.S. acknowledges support from the Israel Science Foundation (ISF grant 1183/13). XAS data were collected on beamline 7-3 at the Stanford Synchrotron Radiation Laboratory (SSRL). Use of the Stanford Synchrotron Radiation Lightsource, SLAC National Accelerator Laboratory, is supported by the U.S. Department of Energy, Office of Science, Office of Basic Energy Sciences, under Contract No. DE-AC02-76SF00515. The SSRL Structural Molecular Biology Program is supported by the DOE Office of Biological and Environmental Research and by the National Institutes of Health, National Institute of General Medical Sciences (including P41GM103393). We are grateful to Dr. Matthew Latimer for his excellent technical support of our XAS experiments and to Dr. Victor G. Young, Jr., for carrying out X-ray crystallographic data collection and structure solutions at the X-ray Crystallographic Laboratory, Department of Chemistry, University of Minnesota. We also thank Prof. Christopher J. Cramer and the Minnesota Supercomputing Institute (MSI) at the University of Minnesota for providing computational resources.

REFERENCES

(1) Kovaleva, E. G.; Lipscomb, J. D. Versatility of biological nonheme Fe(II) centers in oxygen activation reactions. *Nat. Chem. Biol.* **2008**, *4*, 186−193.

(2) Costas, M.; Mehn, M. P.; Jensen, M. P.; Que, L., Jr. Dioxygen Activation at Mononuclear Nonheme Iron Active Sites: Enzymes, Models, and Intermediates. *Chem. Rev.* **2004**, *104*, 939−986.

(3) Koehntop, K. D.; Emerson, J. P.; Que, L., Jr. The 2-His-1-carboxylate facial triad: a versatile platform for dioxygen activation by mononuclear non-heme iron(II) enzymes. *J. Biol. Inorg. Chem.* **2005**, *10*, 87−93.

(4) Hegg, E. L.; Que, L., Jr. The 2-His-1-Carboxylate Facial Triad - An Emerging Structural Motif in Mononuclear Non-Heme Iron(II) Enzymes. *Eur. J. Biochem.* **1997**, *250*, 625−629.

(5) Bruijnincx, P. C. A.; van Koten, G.; Klein Gebbink, R. J. M. Mononuclear non-heme iron enzymes with the 2-His-1-carboxylate facial triad: recent developments in enzymology and modeling studies. *Chem. Soc. Rev.* **2008**, *37*, 2716−2744.

DOI: 10.1021/acs.inorgchem.6b02659
Inorg. Chem. 2017, 56, 3287−3301

(6) Price, J. C.; Barr, E. W.; Tirupati, B.; Bollinger, J. M., Jr.; Krebs, C. The First Direct Characterization of a High-Valent Iron Intermediate in the Reaction of an α-Ketoglutarate-Dependent Dioxygenase: A High-Spin Fe(IV) Complex in Taurine/α-Ketoglutarate Dioxygenase (TauD) from *Escherichia coli*. *Biochemistry* **2003**, *42*, 7497−7508.
(7) Hoffart, L. M.; Barr, E. W.; Guyer, R. B.; Bollinger, J. M., Jr.; Krebs, C. Direct spectroscopic detection of a C-H-cleaving high-spin Fe(IV) complex in a prolyl-4-hydroxylase. *Proc. Natl. Acad. Sci. U. S. A.* **2006**, *103*, 14738−14743.
(8) Eser, B. E.; Barr, E. W.; Frantorn, P. A.; Saleh, L.; Bollinger, J. M., Jr.; Krebs, C.; Fitzpatrick, P. F. Direct Spectroscopic Evidence for a High-Spin Fe(IV) Intermediate in Tyrosine Hydroxylase. *J. Am. Chem. Soc.* **2007**, *129*, 11334−11335.
(9) Matthews, M. L.; Krest, C. M.; Barr, E. W.; Vaillancourt, F. H.; Walsh, C. T.; Green, M. T.; Krebs, C.; Bollinger, J. M., Jr. Substrate-Triggered Formation and Remarkable Stability of the C-H Bond-Cleaving Chloroferryl Intermediate in the Aliphatic Halogenase, SyrB2. *Biochemistry* **2009**, *48*, 4331−4343.
(10) Panay, A. J.; Lee, M.; Krebs, C.; Bollinger, J. M., Jr.; Fitzpatrick, P. F. Evidence for a High-Spin Fe(IV) Species in the Catalytic Cycle of a Bacterial Phenylalanine Hydroxylase. *Biochemistry* **2011**, *50*, 1928−1933.
(11) Galonić, D. P.; Barr, E. W.; Walsh, C. T.; Bollinger, J. M., Jr.; Krebs, C. Two interconverting Fe(IV) intermediates in aliphatic chlorination by the halogenase CytC3. *Nat. Chem. Biol.* **2007**, *3*, 113−116.
(12) Price, J. C.; Barr, E. W.; Glass, T. E.; Krebs, C.; Bollinger, J. M., Jr. Evidence for Hydrogen Abstraction from C1 of Taurine by the High-Spin Fe(IV) Intermediate Detected during Oxygen Activation by Taurine: α-Ketoglutarate Dioxygenase (TauD). *J. Am. Chem. Soc.* **2003**, *125*, 13008−13009.
(13) Riggs-Gelasco, P. J.; Price, J. C.; Guyer, R. B.; Brehm, J. H.; Barr, E. W.; Bollinger, J. M., Jr.; Krebs, C. EXAFS Spectroscopic Evidence for an Fe=O Unit in the Fe(IV) Intermediate Observed during Oxygen Activation by Taurine: α-Ketoglutarate Dioxygenase. *J. Am. Chem. Soc.* **2004**, *126*, 8108−8109.
(14) Proshlyakov, D. A.; Henshaw, T. F.; Monterosso, G. R.; Ryle, M. J.; Hausinger, R. P. Direct Detection of Oxygen Intermediates in the Non-Heme Fe Enzyme Taurine/α-Ketoglutarate Dioxygenase. *J. Am. Chem. Soc.* **2004**, *126*, 1022−1023.
(15) Krebs, C.; Fujimori, D. G.; Walsh, C. T.; Bollinger, J. M., Jr. Non-Heme Fe(IV)-Oxo Intermediates. *Acc. Chem. Res.* **2007**, *40*, 484−492.
(16) Roach, P. L.; Clifton, I. J.; Fülöp, V.; Harlos, K.; Barton, G. J.; Hajdu, J.; Andersson, I.; Schofield, C. J.; Baldwin, J. E. Crystal structure of isopenicillin *N* synthase is the first from a new structural family of enzymes. *Nature* **1995**, *375*, 700−704.
(17) Baldwin, J. E.; Clifton, I. J.; Hensgens, C. M. H.; Shibata, N.; Schofield, C. J.; Hajdu, J. Structure of isopenicillin *N* synthase complexed with substrate and the mechanism of penicillin formation. *Nature* **1997**, *387*, 827−830.
(18) Burzlaff, N. I.; Rutledge, P. J.; Clifton, I. J.; Hensgens, C. M. H.; Pickford, M.; Adlington, R. M.; Roach, P. L.; Baldwin, J. E. The reaction cycle of isopenicillin *N* synthase observed by X-ray diffraction. *Nature* **1999**, *401*, 721−724.
(19) Tamanaha, E.; Zhang, B.; Guo, Y.; Chang, W. C.; Barr, E. W.; Xing, G.; St. Clair, J.; Ye, S.; Neese, F.; Bollinger, J. M., Jr.; Krebs, C. Spectroscopic Evidence for the Two C-H-Cleaving Intermediates of *Aspergillus nidulans* Isopenicillin *N* Synthase. *J. Am. Chem. Soc.* **2016**, *138*, 8862−8874.
(20) McDonald, A. R.; Que, L., Jr. High-valent nonheme iron-oxo complexes: Synthesis, structure, and spectroscopy. *Coord. Chem. Rev.* **2013**, *257*, 414−428.
(21) de Visser, S. P.; Rohde, J.-U.; Lee, Y.-M.; Cho, J.; Nam, W. Intrinsic properties and reactivities of mononuclear nonheme iron−oxygen complexes bearing the tetramethylcyclam ligand. *Coord. Chem. Rev.* **2013**, *257*, 381−393.
(22) Kleespies, S. T.; Oloo, W. N.; Mukherjee, A.; Que, L., Jr. C-H Bond Cleavage by Bioinspired Nonheme Oxoiron(IV) Complexes, Including Hydroxylation of *n*-Butane. *Inorg. Chem.* **2015**, *54*, 5053−5064.
(23) Puri, M.; Que, L., Jr. Toward the Synthesis of More Reactive *S* = 2 Non-Heme Oxoiron(IV) Complexes. *Acc. Chem. Res.* **2015**, *48*, 2443−2452.
(24) Klein, J. E. M. N.; Que, L. Biomimetic High-Valent Mononuclear Nonheme Iron-Oxo Chemistry. In *Encyclopedia of Inorganic and Bioinorganic Chemistry (EIBC)*; Wiley: Hoboken, NJ, 2016; DOI: 10.1002/9781119951438.eibc2344.
(25) Sastri, C. V.; Park, M. J.; Ohta, T.; Jackson, T. A.; Stubna, A.; Seo, M. S.; Lee, J.; Kim, J.; Kitagawa, T.; Münck, E.; Que, L., Jr.; Nam, W. Axial Ligand Substituted Nonheme Fe^{IV}=O Complexes: Observation of Near-UV LMCT Bands and Fe=O Raman Vibrations. *J. Am. Chem. Soc.* **2005**, *127*, 12494−12495.
(26) Sastri, C. V.; Lee, J.; Oh, K.; Lee, Y. J.; Lee, J.; Jackson, T. A.; Ray, K.; Hirao, H.; Shin, W.; Halfen, J. A.; Kim, J.; Que, L., Jr.; Shaik, S.; Nam, W. Axial ligand tuning of a nonheme iron(IV)−oxo unit for hydrogen atom abstraction. *Proc. Natl. Acad. Sci. U. S. A.* **2007**, *104*, 19181−19186.
(27) Jackson, T. A.; Rohde, J.-U.; Seo, M. S.; Sastri, C. V.; DeHont, R.; Stubna, A.; Ohta, T.; Kitagawa, T.; Münck, E.; Nam, W.; Que, L., Jr. Axial Ligand Effects on the Geometric and Electronic Structures of Nonheme Oxoiron(IV) Complexes. *J. Am. Chem. Soc.* **2008**, *130*, 12394−12407.
(28) England, J.; Bigelow, J. O.; Van Heuvelen, K. M.; Farquhar, E. R.; Martinho, M.; Meier, K. K.; Frisch, J. R.; Münck, E.; Que, L., Jr. An ultra-stable oxoiron(iv) complex and its blue conjugate base. *Chem. Sci.* **2014**, *5*, 1204−1215.
(29) Prakash, J.; Rohde, G. T.; Meier, K. K.; Münck, E.; Que, L., Jr. Upside Down! Crystallographic and Spectroscopic Characterization of an $[Fe^{IV}(O_{syn})(TMC)]^{2+}$ Complex. *Inorg. Chem.* **2015**, *54*, 11055−11057.
(30) Mandal, D.; Ramanan, R.; Usharani, D.; Janardanan, D.; Wang, B.; Shaik, S. How Does Tunneling Contribute to Counterintuitive H-Abstraction Reactivity of Nonheme Fe(IV)O Oxidants with Alkanes? *J. Am. Chem. Soc.* **2015**, *137*, 722−733.
(31) Hirao, H.; Que, L., Jr.; Nam, W.; Shaik, S. A Two-State Reactivity Rationale for Counterintuitive Axial Ligand Effects on the C-H Activation Reactivity of Nonheme Fe^{IV}=O Oxidants. *Chem. - Eur. J.* **2008**, *14*, 1740−1756.
(32) Schröder, D.; Shaik, S.; Schwarz, H. Two-State Reactivity as a New Concept in Organometallic Chemistry. *Acc. Chem. Res.* **2000**, *33*, 139−145.
(33) Shaik, S.; Hirao, H.; Kumar, D. Reactivity of High-Valent Iron-Oxo Species in Enzymes and Synthetic Reagents: A Tale of Many States. *Acc. Chem. Res.* **2007**, *40*, 532−542.
(34) Shaik, S. An anatomy of the two-state reactivity concept: Personal reminiscences in memoriam of Detlef Schröder. *Int. J. Mass Spectrom.* **2013**, *354*−*355*, 5−14.
(35) Shaik, S.; Chen, H.; Janardanan, D. Exchange-enhanced reactivity in bond activation by metal-oxo enzymes and synthetic reagents. *Nat. Chem.* **2011**, *3*, 19−27.
(36) Saltzman, H.; Sharefin, J. G. Iodosobenzene. *Org. Synth.* **1963**, *43*, 60−61.
(37) Hagadorn, J. R.; Que, L., Jr.; Tolman, W. B. N-Donor Effects on Carboxylate Binding in Mononuclear Iron(II) Complexes of a Sterically Hindered Benzoate Ligand. *Inorg. Chem.* **2000**, *39*, 6086−6090.
(38) Hagen, K. S. Iron(II) Triflate Salts as Convenient Substitutes for Perchlorate Salts: Crystal Structures of $[Fe(H_2O)_6](CF_3SO_3)_2$ and $Fe(MeCN)_4(CF_3SO_3)_2$. *Inorg. Chem.* **2000**, *39*, 5867−5869.
(39) Yang, W.; Giandomenico, C. M.; Sartori, M.; Moore, D. A. Facile N-1 protection of cyclam, cyclen and 1,4,7-triazacyclononane. *Tetrahedron Lett.* **2003**, *44*, 2481−2483.
(40) Halfen, J. A.; Young, V. G., Jr. Efficient preparation of 1,4,8-trimethylcyclam and its conversion into a thioalkyl-pendant pentadentate chelate. *Chem. Commun.* **2003**, 2894−2895.
(41) Berry, J. F.; Bill, E.; Bothe, E.; Weyhermüller, T.; Wieghardt, K. Octahedral Non-Heme Non-Oxo Fe(IV) Species Stabilized by a

DOI: 10.1021/acs.inorgchem.6b02659
Inorg. Chem. 2017, 56, 3287−3301

Redox-Innocent N-Methylated Cyclam−Acetate Ligand. *J. Am. Chem. Soc.* **2005**, *127*, 11550−11551.
(42) Ramirez, A. L. B.; Kean, Z. S.; Orlicki, J. A.; Champhekar, M.; Elsakr, S. M.; Krause, W. E.; Craig, S. L. Mechanochemical strengthening of a synthetic polymer in response to typically destructive shear forces. *Nat. Chem.* **2013**, *5*, 757−761.
(43) Rohde, J.-U.; In, J.-H.; Brennessel, W. W.; Bukowski, M. R.; Stubna, A.; Münck, E.; Nam, W.; Que, L., Jr. Crystallographic and Spectroscopic Characterization of a Nonheme Fe(IV)═O Complex. *Science* **2003**, *299*, 1037−1039.
(44) Rabideau, P. W.; Mooney, J. L.; Lipkowitz, K. B. Conformational Analysis of 9,10-Dihydroanthracenes. Molecular Mechanics Calculations and ^{13}C NMR. *J. Am. Chem. Soc.* **1986**, *108*, 8130−8134.
(45) Xue, G.; De Hont, R.; Münck, E.; Que, L., Jr. Million-fold activation of the $[Fe_2(\mu\text{-}O)_2]$ diamond core for C-H bond cleavage. *Nat. Chem.* **2010**, *2*, 400−405.
(46) *APEX2*; Bruker AXS, Madison, WI, 2011.
(47) Blessing, R. H. An Empirical Correction for Absorption Anitrosopy. *Acta Crystallogr., Sect. A: Found. Crystallogr.* **1995**, *51*, 33−38.
(48) *SAINT*; Bruker Analytical X-Ray Systems, Madison, WI, 2013.
(49) *SHELXTL V2008/4*; Bruker Analytical X-Ray Systems, Madison, WI, 2008.
(50) George, G. N. *EXAFSPAK*; Stanford Synchrotron Radiation Laboratory, Stanford Linear Accelerator Center, Stanford, CA, 2000.
(51) Wojdyr, M. Fityk: a general-purpose peak fitting program. *J. Appl. Crystallogr.* **2010**, *43*, 1126−1128.
(52) Ankudinov, A. L.; Ravel, B.; Rehr, J. J.; Conradson, S. D. Real-space multiple-scattering calculation and interpretation of x-ray-absorption near-edge structure. *Phys. Rev. B: Condens. Matter Mater. Phys.* **1998**, *58*, 7565−7576.
(53) Becke, A. D. Densityfunctional thermochemistry. III. The role of exact exchange. *J. Chem. Phys.* **1993**, *98*, 5648−5652.
(54) Lee, C.; Yang, W.; Parr, R. G. Development of the Colle-Salvetti correlation-energy formula into a functional of the electron density. *Phys. Rev. B: Condens. Matter Mater. Phys.* **1988**, *37*, 785−789.
(55) Johansson, A. J.; Blomberg, M. R. A.; Siegbahn, P. E. M. Quantifying the effects of the self-interaction error in density functional theory: When do the delocalized states appear? II. Iron-oxo complexes and closed-shell substrate molecules. *J. Chem. Phys.* **2008**, *129*, 154301.
(56) Johansson, A. J.; Blomberg, M. R. A.; Siegbahn, P. E. M. Quantum Chemical Modeling of the Oxidation of Dihydroanthracene by the Biomimetic Nonheme Iron Catalyst $[(TMC)Fe^{IV}(O)]^{2+}$. *J. Phys. Chem. C* **2007**, *111*, 12397−12406.
(57) Janardanan, D.; Usharani, D.; Chen, H.; Shaik, S. Modeling C−H Abstraction Reactivity of Nonheme Fe(IV)O Oxidants with Alkanes: What Role Do Counter Ions Play? *J. Phys. Chem. Lett.* **2011**, *2*, 2610−2617.
(58) Hariharan, P. C.; Pople, J. A. The Influence of Polarization Functions on Molecular Orbital Hydrogenation Energies. *Theor. Chim. Acta* **1973**, *28*, 213−222.
(59) Francl, M. M.; Pietro, W. J.; Hehre, W. J.; Binkley, J. S.; Gordon, M. S.; DeFrees, D. J.; Pople, J. A. Self-consistent molecular orbital methods. XXIII. A polarization-type basis set for second-row elements. *J. Chem. Phys.* **1982**, *77*, 3654−3665.
(60) Hay, P. J.; Wadt, W. R. Ab initio effective core potentials for molecular calculations. Potentials for K to Au including the outermost core orbitals. *J. Chem. Phys.* **1985**, *82*, 299−310.
(61) *Jaguar, Version 8.0*; Schrödinger, LLC, New York, NY, 2011.
(62) Bochevarov, A. D.; Harder, E.; Hughes, T. F.; Greenwood, J. R.; Braden, D. A.; Philipp, D. M.; Rinaldo, D.; Halls, M. D.; Zhang, J.; Friesner, R. A. Jaguar: A High-Performance Quantum Chemistry Software Program with Strengths in Life and Materials Sciences. *Int. J. Quantum Chem.* **2013**, *113*, 2110−2142.
(63) Weigend, F.; Ahlrichs, R. Balanced basis sets of split valence, triple zeta valence and quadruple zeta valence quality for H to Rn: Design and assessment of accuracy. *Phys. Chem. Chem. Phys.* **2005**, *7*, 3297−3305.
(64) Marenich, A. V.; Cramer, C. J.; Truhlar, D. G. Universal Solvation Model Based on Solute Electron Density and on a Continuum Model of the Solvent Defined by the Bulk Dielectric Constant and Atomic Surface Tensions. *J. Phys. Chem. B* **2009**, *113*, 6378−6396.
(65) Frisch, M. J.; Trucks, G. W.; Schlegel, H. B.; Scuseria, G. E.; Robb, M. A.; Cheeseman, J. R.; Scalmani, G.; Barone, V.; Mennucci, B.; Petersson, G. A.; Nakatsuji, H.; Caricato, M.; Li, X.; Hratchian, H. P.; Izmaylov, A. F.; Bloino, J.; Zheng, G.; Sonnenberg, J. L.; Hada, M.; Ehara, M.; Toyota, K.; Fukuda, R.; Hasegawa, J.; Ishida, M.; Nakajima, T.; Honda, Y.; Kitao, O.; Nakai, H.; Vreven, T.; Montgomery, J. A., Jr.; Peralta, J. E.; Ogliaro, F.; Bearpark, M. J.; Heyd, J.; Brothers, E. N.; Kudin, K. N.; Staroverov, V. N.; Kobayashi, R.; Normand, J.; Raghavachari, K.; Rendell, A. P.; Burant, J. C.; Iyengar, S. S.; Tomasi, J.; Cossi, M.; Rega, N.; Millam, N. J.; Klene, M.; Knox, J. E.; Cross, J. B.; Bakken, V.; Adamo, C.; Jaramillo, J.; Gomperts, R.; Stratmann, R. E.; Yazyev, O.; Austin, A. J.; Cammi, R.; Pomelli, C.; Ochterski, J. W.; Martin, R. L.; Morokuma, K.; Zakrzewski, V. G.; Voth, G. A.; Salvador, P.; Dannenberg, J. J.; Dapprich, S.; Daniels, A. D.; Farkas, Ö.; Foresman, J. B.; Ortiz, J. V.; Cioslowski, J.; Fox, D. J. *Gaussian 09*; Gaussian, Inc., Wallingford, CT, USA, 2009.
(66) TURBOMOLE V7.0.1 2015, a development of University of Karlsruhe and Forschungszentrum Karlsruhe GmbH, 1989−2007, TURBOMOLE GmbH, since 2007; available from http://www.turbomole.com.
(67) Furche, F.; Ahlrichs, R.; Hättig, C.; Klopper, W.; Sierka, M.; Weigend, F. Turbomole. *WIREs Comput. Mol. Sci.* **2014**, *4*, 91−100.
(68) Ahlrichs, R.; Bär, M.; Häser, M.; Horn, H.; Kölmel, C. Electronic structure calculations on workstation computers: The program system turbomole. *Chem. Phys. Lett.* **1989**, *162*, 165−169.
(69) Klamt, A.; Schüürmann, G. COSMO: a new approach to dielectric screening in solvents with explicit expressions for the screening energy and its gradient. *J. Chem. Soc., Perkin Trans. 2* **1993**, 799−805.
(70) Klamt, A.; Jonas, V. Treatment of the outlying charge in continuum solvation models. *J. Chem. Phys.* **1996**, *105*, 9972−9981.
(71) Atwood, D. A.; Hutchison, A. R.; Zhang, Y. Compounds Containing Five-Coordinate Group 13 Elements; In *Group 13 Chemistry III: Industrial Applications*; Roesky, H. W., Atwood, D. A., Eds.; Springer: Berlin, Heidelberg, 2003; pp 167−201.
(72) Fiedler, A. T.; Halfen, H. L.; Halfen, J. A.; Brunold, T. C. Synthesis, Structure Determination, and Spectroscopic/Computational Characterization of a Series of Fe(II)−Thiolate Model Complexes: Implications for Fe−S Bonding in Superoxide Reductases. *J. Am. Chem. Soc.* **2005**, *127*, 1675−1689.
(73) McDonald, A. R.; Bukowski, M. R.; Farquhar, E. R.; Jackson, T. A.; Koehntop, K. D.; Seo, M. S.; De Hont, R. F.; Stubna, A.; Halfen, J. A.; Münck, E.; Nam, W.; Que, L., Jr. Sulfur versus Iron Oxidation in an Iron-Thiolate Model Complex. *J. Am. Chem. Soc.* **2010**, *132*, 17118−17129.
(74) Thibon, A.; England, J.; Martinho, M.; Young, V. G., Jr.; Frisch, J. R.; Guillot, R.; Girerd, J.-J.; Münck, E.; Que, L., Jr.; Banse, F. Proton- and Reductant-Assisted Dioxygen Activation by a Nonheme Iron(II) Complex to Form an Oxoiron(IV) Intermediate. *Angew. Chem., Int. Ed.* **2008**, *47*, 7064−7067.
(75) Hodges, K. D.; Wollmann, R. G.; Kessel, S. L.; Hendrickson, D. N.; Van Derveer, D. G.; Barefield, E. K. Preparations and Properties of Nitrosyl Complexes of Iron Tetramethylcyclam. X-ray Structures of $[Fe(C_{14}H_{32}N_4)NO](BF_4)_2$, a $S = 3/2-1/2$ Spin-Equilibrium Complex, and $[Fe(C_{14}H_{32}N_4)(NO)(OH)](ClO_4)_2.CH_3CN$. *J. Am. Chem. Soc.* **1979**, *101*, 906−917.
(76) Wilson, S. A.; Chen, J.; Hong, S.; Lee, Y.-M.; Clemancey, M.; Garcia-Serres, R.; Nomura, T.; Ogura, T.; Latour, J.-M.; Hedman, B.; Hodgson, K. O.; Nam, W.; Solomon, E. I. $[Fe^{IV}═O(TBC)(CH_3CN)]^{2+}$: Comparative Reactivity of Iron(IV)-Oxo Species with Constrained Equatorial Cyclam Ligation. *J. Am. Chem. Soc.* **2012**, *134*, 11791−11806.

DOI: 10.1021/acs.inorgchem.6b02659
Inorg. Chem. 2017, 56, 3287−3301

(77) Barefield, E. K. Coordination chemistry of N-tetraalkylated cyclam ligands—A status report. *Coord. Chem. Rev.* **2010**, *254*, 1607−1627.
(78) Macrae, C. F.; Edgington, P. R.; McCabe, P.; Pidcock, E.; Shields, G. P.; Taylor, R.; Towler, M.; van de Streek, J. *Mercury*: visualization and analysis of crystal structures. *J. Appl. Crystallogr.* **2006**, *39*, 453−457.
(79) Macrae, C. F.; Bruno, I. J.; Chisholm, J. A.; Edgington, P. R.; McCabe, P.; Pidcock, E.; Rodriguez-Monge, L.; Taylor, R.; van de Streek, J.; Wood, P. A. *Mercury CSD 2.0* - new features for the visualization and investigation of crystal structures. *J. Appl. Crystallogr.* **2008**, *41*, 466−470.
(80) Decker, A.; Rohde, J.-U.; Que, L., Jr.; Solomon, E. I. Spectroscopic and Quantum Chemical Characterization of the Electronic Structure and Bonding in a Non-Heme Fe^{IV}=O Complex. *J. Am. Chem. Soc.* **2004**, *126*, 5378−5379.
(81) Decker, A.; Rohde, J.-U.; Klinker, E. J.; Wong, S. D.; Que, L., Jr.; Solomon, E. I. Spectroscopic and Quantum Chemical Studies on Low-Spin Fe^{IV}=O Complexes: Fe-O Bonding and Its Contributions to Reactivity. *J. Am. Chem. Soc.* **2007**, *129*, 15983−15996.
(82) Rohde, J.-U.; Que, L., Jr. Axial Coordination of Carboxylate Activates the Non-heme Fe^{IV}=O Unit. *Angew. Chem., Int. Ed.* **2005**, *44*, 2255−2258.
(83) Grapperhaus, C. A.; Mienert, B.; Bill, E.; Weyhermuller, T.; Wieghardt, K. Mononuclear (Nitrido)iron(V) and (Oxo)iron(IV) Complexes via Photolysis of $[(\text{cyclam-acetato})Fe^{III}(N_3)]^+$ and Ozonolysis of $[(\text{cyclam-acetato})Fe^{III}(O_3SCF_3)]^+$ in Water/Acetone Mixtures. *Inorg. Chem.* **2000**, *39*, 5306−5317.
(84) Vad, M. S.; Lennartson, A.; Nielsen, A.; Harmer, J.; McGrady, J. E.; Frandsen, C.; Morup, S.; McKenzie, C. J. An aqueous non-heme Fe(IV)oxo complex with a basic group in the second coordination sphere. *Chem. Commun.* **2012**, *48*, 10880−10882.
(85) Wang, D.; Ray, K.; Collins, M. J.; Farquhar, E. R.; Frisch, J. R.; Gomez, L.; Jackson, T. A.; Kerscher, M.; Waleska, A.; Comba, P.; Costas, M.; Que, L., Jr. Nonheme oxoiron(IV) complexes of pentadentate N5 ligands: spectroscopy, electrochemistry, and oxidative reactivity. *Chem. Sci.* **2013**, *4*, 282−291.
(86) Morokuma, K. Molecular Orbital Studies of Hydrogen Bonds. III. C=O···H−O Hydrogen Bond in $H_2CO···H_2O$ and $H_2CO···2H_2O$. *J. Chem. Phys.* **1971**, *55*, 1236−1244.
(87) Kitaura, K.; Morokuma, K. A New Energy Decomposition Scheme for Molecular Interactions Within the Hartree-Fock Approximation. *Int. J. Quantum Chem.* **1976**, *10*, 325−340.
(88) Ziegler, T.; Rauk, A. On the Calculation of Bonding Energies by the Hartree Fock Slater Method. *Theor. Chim. Acta* **1977**, *46*, 1−10.
(89) Ziegler, T.; Rauk, A. A Theoretical Study of the Ethylene-Metal Bond in Complexes between Cu^+, Ag^+, Au^+, Pt^0 or Pt^{2+} and Ethylene, Based on the Hartree-Fock-Slater Transition-State Method. *Inorg. Chem.* **1979**, *18*, 1558−1565.
(90) Strozier, R. W.; Caramella, P.; Houk, K. N. Influence of Molecular Distortions upon Reactivity and Stereochemistry in Nucleophilic Additions to Acetylenes. *J. Am. Chem. Soc.* **1979**, *101*, 1340−1343.
(91) Mitchell, D. J.; Schlegel, H. B.; Shaik, S. S.; Wolfe, S. Relationships between geometries and energies of identity S_N2 transition states: the dominant role of the distortion energy and its origin. *Can. J. Chem.* **1985**, *63*, 1642−1648.
(92) Guthrie, J. P. No-Barrier Theory: Calculating Rates of Chemical Reactions from Equilibrium Constants and Distortion Energies. *ChemPhysChem* **2003**, *4*, 809−816.
(93) Ess, D. H.; Houk, K. N. Distortion/Interaction Energy Control of 1,3-Dipolar Cycloaddition Reactivity. *J. Am. Chem. Soc.* **2007**, *129*, 10646−10647.
(94) Legault, C. Y.; Garcia, Y.; Merlic, C. A.; Houk, K. N. Origin of Regioselectivity in Palladium-Catalyzed Cross-Coupling Reactions of Polyhalogenated Heterocycles. *J. Am. Chem. Soc.* **2007**, *129*, 12664−12665.
(95) Ess, D. H.; Houk, K. N. Theory of 1,3-Dipolar Cycloadditions: Distortion/Interaction and Frontier Molecular Orbital Models. *J. Am. Chem. Soc.* **2008**, *130*, 10187−10198.
(96) van Zeist, W.-J.; Bickelhaupt, F. M. The activation strain model of chemical reactivity. *Org. Biomol. Chem.* **2010**, *8*, 3118−3127.
(97) Diefenbach, A.; Bickelhaupt, F. M. Activation of H−H, C−H, C−C, and C−Cl Bonds by Pd(0). Insight from the Activation Strain Model. *J. Phys. Chem. A* **2004**, *108*, 8460−8466.
(98) Shaik, S.; Lai, W.; Chen, H.; Wang, Y. The Valence Bond Way: Reactivity Patterns of Cytochrome P450 Enzymes and Synthetic Analogs. *Acc. Chem. Res.* **2010**, *43*, 1154−1165.
(99) Usharani, D.; Lai, W.; Li, C.; Chen, H.; Danovich, D.; Shaik, S. A tutorial for understanding chemical reactivity through the valence bond approach. *Chem. Soc. Rev.* **2014**, *43*, 4968−4988.
(100) Yi, W.; Yuan, L.; Kun, Y.; Zhengwen, H.; Jing, T.; Xu, F.; Hong, G.; Yong, W. What factors influence the reactivity of C−H hydroxylation and C=C epoxidation by $[Fe^{IV}(L_{ax})(1,4,8,11\text{-tetramethyl-}1,4,8,11\text{-tetraazacyclotetradecane})(O)]^{n+}$. *JBIC, J. Biol. Inorg. Chem.* **2015**, *20*, 1123−1134.
(101) Chen, J.; Cho, K.-B.; Lee, Y.-M.; Kwon, Y. H.; Nam, W. Mononuclear nonheme iron(IV)-oxo and manganese(IV)-oxo complexes in oxidation reactions: experimental results prove theoretical prediction. *Chem. Commun.* **2015**, *51*, 13094−13097.
(102) Jaccob, M.; Comba, P.; Maurer, M.; Vadivelu, P.; Venuvanalingam, P. A combined experimental and computational study on the sulfoxidation by high-valent iron bispidine complexes. *Dalton Trans.* **2011**, *40*, 11276−11281.
(103) Chang, W.-c.; Li, J.; Lee, J. L.; Cronican, A. A.; Guo, Y. Mechanistic Investigation of a Non-Heme Iron Enzyme Catalyzed Epoxidation in (−)-4′-Methoxycyclopenin Biosynthesis. *J. Am. Chem. Soc.* **2016**, *138*, 10390−10393.

DOI: 10.1021/acs.inorgchem.6b02659
Inorg. Chem. 2017, 56, 3287−3301